The Astrophysical Journal, 802:53 (20pp), 2015 March 20 doi:10.1088/0004-637X/802/1/53

GLOBAL ENERGETICS OF SOLAR FLARES. II. THERMAL ENERGIES

Markus J. Aschwanden[1], Paul Boerner[1], Daniel Ryan[2], Amir Caspi[3], James M. McTiernan[4], and Harry P. Warren[5]
[1] Lockheed Martin, Solar and Astrophysics Laboratory, Org. A021S, Bldg. 252, 3251 Hanover St., Palo Alto, CA 94304, USA; aschwanden@lmsal.com
[2] Royal Observatory of Belgium, Solar-Terrestrial Centre for Excellence, Avenue Circulaire 3, 1180 Uccle, Brussels, Belgium; ryand5@tcd.ie
[3] Planetary Science Directorate, Southwest Research Institute, Boulder, CO 80302, USA; amir.caspi@lasp.colorado.edu
[4] Space Sciences Laboratory, University of California, Berkeley, CA 94720, USA; jimm@ssl.berkeley.edu
[5] Space Science Division, Naval Research Laboratory, Washington, DC 20375, USA; harry.warren@nrl.navy.mil
Received 2014 October 21; accepted 2015 February 18; published 2015 March 20

ABSTRACT

We present the second part of a project on the global energetics of solar flares and coronal mass ejections that includes about 400 M- and X-class flares observed with the Atmospheric Imaging Assembly (AIA) onboard the *Solar Dynamics Observatory* (*SDO*) during the first 3.5 yr of its mission. In this Paper II we compute the differential emission measure (DEM) distribution functions and associated multithermal energies, using a spatially-synthesized Gaussian DEM forward-fitting method. The multithermal DEM function yields a significantly higher (by an average factor of ≈14), but more comprehensive (multi-)thermal energy than an isothermal energy estimate from the same AIA data. We find a statistical energy ratio of $E_{\rm th}/E_{\rm diss} \approx 2$–40% between the multithermal energy $E_{\rm th}$ and the magnetically dissipated energy $E_{\rm diss}$, which is an order of magnitude higher than the estimates of Emslie et al. 2012. For the analyzed set of M- and X-class flares we find the following physical parameter ranges: $L = 10^{8.2}$–$10^{9.7}$ cm for the length scale of the flare areas, $T_p = 10^{5.7}$–$10^{7.4}$ K for the DEM peak temperature, $T_w = 10^{6.8}$–$10^{7.6}$ K for the emission measure-weighted temperature, $n_p = 10^{10.3}-10^{11.8}$ cm^{-3} for the average electron density, $\mathrm{EM}_p = 10^{47.3}$–$10^{50.3}$ cm^{-3} for the DEM peak emission measure, and $E_{\rm th} = 10^{26.8}$–$10^{32.0}$ erg for the multithermal energies. The deduced multithermal energies are consistent with the RTV scaling law $E_{\rm th,RTV} = 7.3 \times 10^{-10}\, T_p^3 L_p^2$, which predicts extremal values of $E_{\rm th,max} \approx 1.5 \times 10^{33}$ erg for the largest flare and $E_{\rm th,min} \approx 1 \times 10^{24}$ erg for the smallest coronal nanoflare. The size distributions of the spatial parameters exhibit powerlaw tails that are consistent with the predictions of the fractal-diffusive self-organized criticality model combined with the RTV scaling law.

Key words: plasmas – radiation mechanisms: thermal – Sun: flares – Sun: UV radiation

Supporting material: machine-readable table

1. INTRODUCTION

While we measured the magnetic energy that is dissipated in large solar flares in Paper I (Aschwanden et al. 2014a), the goal of this paper II is the determination of thermal energies of the heated flare plasma, in order to study the energy partition of the input (magnetic) energy into various output (thermal and other) energies. A crucial test is the thermal to magnetic energy ratio, which is expected to be less than unity for magnetic energy release processes (such as magnetic reconnection). Ratios in excess of unity would indicate either inaccurate energy measurements of either magnetic or thermal energies, or would challenge standard flare scenarios where the source of dissipated energy is entirely of magnetic origin. In the standard CSHKP magnetic reconnection model (Carmichael 1964; Sturrock 1966; Hirayama 1974; Kopp & Pneuman 1976), magnetic reconnection drives the nonlinear dissipation of magnetic energy, which is then converted partially into particle acceleration and (precipitation-driven and conduction-driven) flare plasma heating, for which the thermal energy is naturally expected to be a fraction of the total dissipated magnetic energy only. Thus, statistical measurements of the thermal to magnetic energy ratio provide crucial tests for theoretical flare scenarios as well as on the accuracy of observational flare energy measurement methods.

The problematics of determining magnetic energies has been discussed extensively in Paper I. There are three forms of magnetic energies: the potential energy, the free energy (or excess of nonpotential over potential energy), and the dissipated energy, which corresponds to the negative change of free energy during a flare event. Therefore, the measurement of dissipated magnetic energies requires methods that can accurately detect deviations from the potential magnetic field, which are difficult to achieve, as a quantitative comparison of 12 nonlinear force-free field (NLFFF) extrapolation methods of the photospheric magnetic field demonstrated (DeRosa et al. 2009). Alternative NLFFF methods that use the geometry of (automatically traced) coronal loops as constraints appear to be more promising for this task (Paper I). There exists only one study that attempts to compare dissipated magnetic energies with thermal energies in a set of (large eruptive) flare events (Emslie et al. 2012), but the dissipated magnetic energy could not be determined in that study and instead was estimated to amount to $E_{\rm diss}/E_p \approx 30\%$ of the potential energy, leading to a rather small thermal/magnetic energy ratio, on the order of $E_{\rm th}/E_{\rm diss} \approx 0.2$–1%. Since the ratio of the dissipated magnetic energy $E_{\rm diss}$ to the potential magnetic energy E_p has been found to have a substantially smaller value in Paper I, in the range of $E_{\rm diss}/E_p \approx 1$–25% for a representative set of M- and X-class flares, we suspect that the thermal/magnetic energy ratio is systematically underestimated in the study of Emslie et al. (2012). As a consequence, we will see in the present study that the thermal/magnetic energy ratio in large solar flares is indeed significantly higher than previously inferred in Emslie et al. (2012).

Table 1
Thermal Energy Parameters of 28 X-class Flare Events

#	Flare Start Time	GOES Class	Helio-Graphic Position	Length Scale L (Mm)	Peak Temperature T_p (MK)	EM-weighted Temperature T_w (MK)	Electron Density log (n_e) (cm^{-3})	Emission Measure log(EM) (cm^{-3})	Thermal Energy E_{th} (10^{30} erg)
12	20110215 0144	X2.2	S21W12	28.4	15.9	27.9	10.8	49.9	82.2
37	20110309 2313	X1.5	N10W11	34.8	5.6	22.5	10.6	49.7	84.7
61	20110809 0748	X6.9	N14W69	28.9	15.9	28.4	10.9	50.2	128.9
66	20110906 2212	X2.1	N16W15	24.5	15.9	25.4	10.8	49.7	52.2
67	20110907 2232	X1.8	N16W30	37.4	28.2	28.9	10.6	50.0	140.6
107	20111103 2016	X1.9	N21E64	26.2	25.1	33.2	10.8	49.8	76.4
132	20120127 1737	X1.7	N33W85	46.0	6.3	14.8	10.4	49.8	107.3
136	20120305 0230	X1.1	N19E58	29.7	14.1	33.9	10.7	49.8	92.9
147	20120307 0002	X5.4	N18E31	44.9	14.1	21.8	10.6	50.3	208.4
148	20120307 0105	X1.3	N18E29	36.0	4.0	22.7	10.5	49.7	89.8
209	20120706 2301	X1.1	S13W59	20.4	5.6	28.5	10.8	49.5	33.2
220	20120712 1537	X1.4	S15W03	36.3	6.3	24.2	10.6	49.8	105.3
248	20121023 0313	X1.8	S13E58	10.4	15.9	34.1	11.1	49.4	11.5
286	20130513 1548	X2.8	N08E89	23.6	17.8	33.3	10.9	49.9	70.9
287	20130514 0000	X3.2	N08E77	29.9	15.9	28.5	10.8	50.1	109.5
288	20130515 0125	X1.2	N10E68	22.6	5.6	27.1	10.7	49.5	40.8
318	20131025 0753	X1.7	S08E73	11.4	28.2	29.1	11.1	49.3	10.9
320	20131025 1451	X2.1	S06E69	17.0	4.0	30.5	10.9	49.4	24.6
330	20131028 0141	X1.0	N05W72	15.9	15.9	32.0	10.9	49.5	23.3
337	20131029 2142	X2.3	N05W87	23.9	22.4	30.3	10.8	49.8	53.7
344	20131105 2207	X3.3	S08E44	12.0	25.1	32.8	11.1	49.4	14.7
349	20131108 0420	X1.1	S11E11	20.8	25.1	30.2	10.9	49.8	43.0
351	20131110 0508	X1.1	S13W13	22.0	17.8	33.3	10.9	49.8	54.5
358	20131119 1014	X1.0	S13W69	18.3	20.0	30.7	10.9	49.6	31.4
384	20140107 1804	X1.2	S12E08	3.0	1.8	25.1	11.4	48.2	0.4

Even if we have an accurate method to determine the dissipated magnetic energy in solar flares, there are also large uncertainties in the determination of the thermal energy due to the inhomogeneity and multithermal nature of the solar flare plasma. In principle, an accurate measure of the multithermal energy could be determined if the full 3D distribution of electron temperatures $T_e(x, y, z)$ and electron densities $n_e(x, y, z)$ are known, such as produced in 3D magneto-hydrodynamic (MHD) simulations (e.g., Testa et al. 2012). In practice, we have only 2D images in multiple wavelengths available to determine the thermal energy. While the lateral extent (in the $[x,y]$-plane) of flare-related emission in EUV and soft X-rays can be accurately measured for instruments with high spatial resolution, such as with the Atmospheric Imaging Assembly (AIA)/*Solar Dynamics Observatory* (*SDO*), the line-of-sight column depth (in the $[z]$-direction) is subject to geometric models. Moreover, the differential emission measure (DEM) distribution can only be determined as an integral along any line-of-sight, and thus the thermal inhomogeneity and filling factors along the line-of-sight add additional uncertainties. Nevertheless, the currently available high-resolution and multi-wavelength capabilities of AIA/SDO provide unprecedented possibilities to model the 3D flare plasma distribution with much higher fidelity than previous instruments from the *SMM*, *SOHO*, *TRACE*, and *STEREO* missions. It is therefore timely to attempt a statistical study of magnetic and thermal energies using AIA and HMI data from the *SDO*.

The content of this Paper II includes a description of the data analysis methods to determine multithermal flare energies (Section 2 and Appendix), a presentation of observations and results (Section 3 and Tables 1 and 2), discussions of problems pertinent to the determination of thermal energies (Section 4), and conclusions about thermal and magnetic flare energies (Section 5).

2. DATA ANALYSIS METHODS

2.1. AIA/SDO Temperature Filters

The temperature and density analysis carried out here uses EUV images from the AIA (Boerner et al. 2012; Lemen et al. 2012) onboard the *SDO* spacecraft (Pesnell et al. 2011). AIA contains 10 different wavelength channels, three in white light and UV, and seven EUV channels, whereof six wavelengths (94, 131, 171, 193, 211, 335 Å) are centered on strong iron lines (Fe VIII, IX, XII, XIV, XVI, XVIII), covering the coronal range from $T \approx 0.6$ to $\gtrsim$16 MK. The 304 Å (He II) filter was not used because it is mostly sensitive to chromospheric temperatures of $T_e \approx 10^{4.7}$, which is outside of the range of interest for the flare study here. The calibration of the response functions has changed somewhat over time. Early on in the mission, the response of the 94 and 131 Å channels was underestimated (see Figure 10 in Aschwanden & Boerner 2011). Here we will use the currently available calibration, which was updated with improved atomic emissivities according to the CHIANTI Version 7 code, distributed in the *Solar SoftWare (SSW)* on 2012 February 13.

2.2. Gaussian Differential Emission Measure Distribution Function

The measurement of the thermal energy $E_{th} = 3n_e k_B T_e V$ of an (isothermal) flare plasma requires the determination of the electron density n_e, the electron temperature T_e, and the flare volume V. From multi-wavelength observations it is customary

Table 2
Thermal Energy Parameters of 391 M- and X-Class Flare Events

#	Flare Start Time	GOES Class	Helio-Graphic Position	Length Scale L (Mm)	Peak Temperature T_p (MK)	EM-weighted Temperature T_w (MK)	Electron Density log (n_e) (cm^{-3})	Emission Measure log(EM) (cm^{-3})	Thermal Energy E_{th} (10^{30} erg)
1	20100612 0030	M2.0	N23W47	13.2	6.3	18.6	10.8	48.9	7.0
2	20100613 0530	M1.0	S24W82	12.2	7.1	15.8	10.7	48.6	4.1
3	20100807 1755	M1.0	N13E34	25.1	4.0	6.2	10.4	49.1	8.2
4	20101016 1907	M2.9	S18W26	15.1	14.1	29.9	10.9	49.4	19.2
5	20101104 2330	M1.6	S20E85	13.8	10.0	24.9	10.8	49.0	10.2
6	20101105 1243	M1.0	S20E75	13.3	6.3	19.8	10.8	48.9	7.7
7	20101106 1527	M5.4	S20E58	20.3	4.0	20.9	10.7	49.4	24.6
9	20110209 0123	M1.9	N16W70	8.2	3.2	28.5	11.0	48.7	3.4
10	20110213 1728	M6.6	S21E04	15.9	14.1	23.9	10.9	49.5	20.8
…	…	…	…	…	…	…	…	…	…

(This table is available in its entirety in machine-readable form.)

to calculate the DEM distribution function, which can be integrated over the coronal temperature range and yields a total emission measure $\mathrm{EM} = n_e^2\, V$, providing a mean electron density n_e (for unity filling factor) and a mean DEM peak temperature T_e. The inference of the DEM can be accomplished either by inversion of the observed fluxes using the instrumental response functions, or by forward-fitting of a suitable functional form of a DEM distribution function. DEM inversion methods are often unstable (Craig & Brown 1976; Judge et al. 1997; Testa et al. 2012; M. J. Aschwanden et al. 2015, in preparation), while forward-fitting methods are generally more robust, but require a suitable parameterization of an analytical function that has to satisfy an acceptable goodness-of-fit criterion. A comparison of 10 DEM inversion and forward-fitting methods has been conducted in a recent study with simulated DEMs, using AIA, *EVE, RHESSI*, and *GOES* response functions (M. J. Aschwanden et al. 2015, in preparation), where the performance of recent DEM methods is discussed in more detail.

One of the most robust choices of a DEM function with a minimum of free parameters is a single Gaussian (in the logarithm of the temperature), which has three free parameters only and is defined by the peak emission measure EM_p, the DEM peak temperature T_p, and the logarithmic temperature width w_T, where the DEM parameter has the cgs-units of $\mathrm{cm}^{-5}\ \mathrm{K}^{-1}$,

$$\mathrm{DEM}(T) = n_e^2 \frac{dz}{dT} = \mathrm{EM}_p \exp\left(-\frac{\left[\log(T) - \log\left(T_p\right)\right]^2}{2w_T^2}\right), \quad (1)$$

where the line-of-sight emission measure $d\mathrm{EM} = n_e^2 dz$ is the temperature integral over the Gaussian DEM (in units of cm^{-5},

$$\mathrm{EM} = \int \mathrm{DEM}(T)\, dT. \quad (2)$$

The Gaussian DEM (Equation (1)) can be forward-fitted to the preflare background-subtracted observed fluxes f_λ in multiple wavelengths λ,

$$f_\lambda(t) = F_\lambda(t) - B_\lambda(t) = \int \mathrm{DEM}(T)\, R_\lambda(T)\, dT = \sum_{k=1}^{n_T} \mathrm{DEM}\left(T_k\right) R_\lambda\left(T_k\right) \Delta T_k, \quad (3)$$

where F_λ are the observed fluxes (in units of $\mathrm{DN\,s^{-1}}$) in the wavelengths $\lambda = 94, 131, 171, 193, 211, 335$ Å, B_λ are the observed background fluxes, f_λ are the background-subtracted fluxes, integrated over the entire flare area, $R_\lambda(T)$ is the instrumental response function of each wavelength filter λ (in units of $\mathrm{DN\ s^{-1}\ cm^5}$ per pixel), and the temperature integration is using discretized temperature intervals ΔT_k, which generally are chosen to be equidistant bins of the logarithmic temperature range.

In our DEM forward-fitting algorithm we use a temperature range of $T_p = 0.5-30$ MK that is subdivided equi-distantly into 36 logarithmic temperature bins ΔT_k, and a Gaussian temperature width range with 10 values in the range of $w_T = 0.1-1.0$. At the same time, the DEM peak emission measure value EM_p is evaluated from the median ratio of the observed to the model (background-subtracted) fluxes,

$$\mathrm{EM}_p = \mathrm{EM}_0 \left[\frac{\sum_\lambda f_\lambda^{\mathrm{obs}}}{\sum_\lambda f_\lambda^{\mathrm{fit}}}\right], \quad (4)$$

where $\mathrm{EM}_0 = 1\ \mathrm{cm^{-5}\,K^{-1}}$ is the unity emission measure. The best-fitting values of the peak emission measure EM_p, the peak temperature T_p and temperature width w_T are found by a global search in the 2-parameter space $[T, w_T]$ and by adjustment of the peak emission measure value EM_p. The best-fit solution is then evaluated by the goodness-of-fit criterion (e.g., Bevington & Robinson 1992),

$$\chi(t) = \left[\frac{1}{n_{\mathrm{free}}} \sum_{\lambda=1}^{n_\lambda} \frac{\left(f_\lambda^{\mathrm{fit}}(t) - f_\lambda^{\mathrm{obs}}(t)\right)^2}{\sigma_\lambda^2(t)}\right]^{1/2}, \quad (5)$$

where $f_\lambda^{\rm obs}$ are the six observed flux values, $f_\lambda^{\rm fit}$ are the flux values of the fitted Gaussian DEM (Equation (1)), σ_λ are the estimated uncertainties, $n_{\rm free} = n_\lambda - n_{\rm par}$ is the number of degrees of freedom, which is $n_{\rm free} = 3$ for $n_\lambda = 6$ the number of wavelength filters and $n_{\rm par} = 3$ the number of model parameters.

In recent studies it is found that the dominant uncertainty in fitting fluxes observed with AIA/*SDO* comes from the incomplete knowledge of the AIA response functions, which concerns missing atomic lines in the CHIANTI code as well as uncertainties whether photospheric or coronal abundances of chemical elements are more appropriate. The combined uncertainty is estimated to be ≈10–25% of the observed AIA fluxes in each wavelength (Testa et al. 2012; Boerner et al. 2014; M. J. Aschwanden et al. 2015, in preparation). This is much more than the typical uncertainty due to photon count statistics, which is of order $\approx 10^{-4} - 10^{-3}$ for typical AIA count rates ($\approx 10^6 - 10^8$ DN s^{-1}) during flares (O'Dwyer et al. 2010; Boerner et al. 2014). We thus perform the DEM forward-fitting to the 6 wavelength fluxes by using the empirical 10% error of the response functions as an estimate of the flux uncertainties due to calibration and background subtraction errors,

$$\sigma_\lambda \approx 0.1\, f_\lambda^{\rm obs}. \quad (6)$$

2.3. Spatial Synthesis of Gaussian DEM Fitting

The choice of a suitable DEM function in forward-fitting methods is almost an art. A Gaussian function (in the logarithm of the temperature) appears to be a good approximation near the peak temperature T_p of most DEM functions, but cannot represent "shoulders" of the primary peak, or secondary peaks at lower or higher temperatures. This is particularly a problem for EUV images that have many different temperature structures with competing emission measures in different areas of the image, such as multiple cores of hot flaring regions, surrounded by peripheral cooler regions. Therefore it is a sensible approach in the DEM parameterization to subdivide the image area of a flare into macropixels or even single pixels, and then to perform a forward-fit of a (single-Gaussian) DEM function in each spatial location separately, while the total DEM distribution function of the entire flare area can then be constructed by summing all DEM functions from each spatial location, which we call the "Spatial Synthesis DEM" method. This way, the Gaussian approximation of a DEM function is applied locally only, but can adjust different peak emission measures and temperatures at each spatial location. Such a single-pixel algorithm for automated temperature and emission measure analysis has been developed for the six coronal AIA wavelength filter images in Aschwanden et al. (2013), and a SSW/IDL code is available online (http://www.lmsal.com/~aschwand/software/aia/aia_dem.html). The flux $F_\lambda(x, y, t)$ is then measured in each pixel location $[x, y]$ and time t, and the fitted DEM functions are defined at each location $[x, y]$ and time t separately,

$$\mathrm{DEM}(T; x, y, t) = \mathrm{EM}_p(x, y, t) \times \exp\left(-\frac{\left[\log(T) - \log\left(T_p[x, y, t]\right)\right]^2}{2w_T^2[x, y, t]}\right), \quad (7)$$

and are forward-fitted to the observed fluxes $F_\lambda(x, y, t)$ at each location (x,y) and time t separately,

$$F_\lambda(x, y, t) - B_\lambda(x, y, t) = \int \mathrm{DEM}(T; x, y, t) R_\lambda(T) dT = \sum_{k=1}^{n_T} \mathrm{DEM}\left(T_k; x_i, y_j, t\right) R_\lambda\left(T_k\right) \Delta T_k. \quad (8)$$

The synthesized differential emission measure distribution DEM(T) can then be obtained by summing up all local DEM distribution functions DEM(T; x, y, t) (in units of cm^{-3} K^{-1}),

$$\mathrm{DEM}(T, t) = \int\int \mathrm{DEM}(T; x, y, t)\, dxdy = \sum_{i,j} \mathrm{DEM}\left(T_k; x_i, y_j, t\right) dx_i dy_j, \quad (9)$$

and the total emission measure of a flaring region is then obtained by integration over the temperature range (in units of cm^{-3}),

$$\mathrm{EM}(t) = \int \mathrm{DEM}(T, t)\, dT = \sum_k \mathrm{DEM}_k\left(T_k, t\right) \Delta T_k. \quad (10)$$

Note that the synthesized DEM function DEM(T) (Equation (9)) generally deviates from a Gaussian shape, because it is constructed from the summation of many Gaussian DEMs from each pixel location with different emission measure peaks $\mathrm{EM}_p(x_i, y_j)$, peak temperatures $T_p(x_i, y_j)$, and thermal widths $w_T(x_i, y_j)$. This synthesized DEM function can be arbitrarily complex and can accomodate a different Gaussian DEM function in every spatial location (x_i, y_j).

Typically we process images with a field-of-view (FOV) of FOV = 0.35 solar radii, which corresponds to about 520 AIA pixels. Subdividing these images into macropixels with a bin size of four full-resolution pixels, we have a grid of 130 × 130 macropixels $[x_i, y_j]$ and perform $130^2 = 16{,}900$ single-Gaussian DEM fits per time frame, per wavelength set, and per event. We illustrate the spatial synthesis procedure with single-Gaussian DEMs in Figure 1, where we can see that the local temperature discrimination yields a higher temperature contrast for increasingly smaller macropixels, from $N_{\rm bin} = 512, 256, 128, 64, 32, 16, 8, 4$ down to 2 image pixels. The convergence of the DEM with decreasing bin size is depicted in Figure 2, for three different times of a flare. The initial single-Gaussian DEM function fitted to the fluxes of a 512 × 512 pixel area (blue curves in Figure 2) converges to a double-peaked DEM at the flare peak time (red curve in middle panel of Figure 2), synthesized from 2 × 2 macropixels, which evolves then into a broad single-peaked DEM in the postflare phase (red curve in the bottom panel of Figure 2).

2.4. Flare Geometry

The total emission measure EM of a flaring active region, such as defined for a single Gaussian DEM (Equation (2)) or for a spatially synthesized DEM as defined in Equation (10), yields the product of the squared mean electron density times the flare volume. If we can estimate the flare volume V from the imaging information, we can then infer the mean electron density (for unity filling factor). There are many ways to measure a flare area. Two major problems are the choice of a suitable wavelength (in multi-temperature data), and secondly

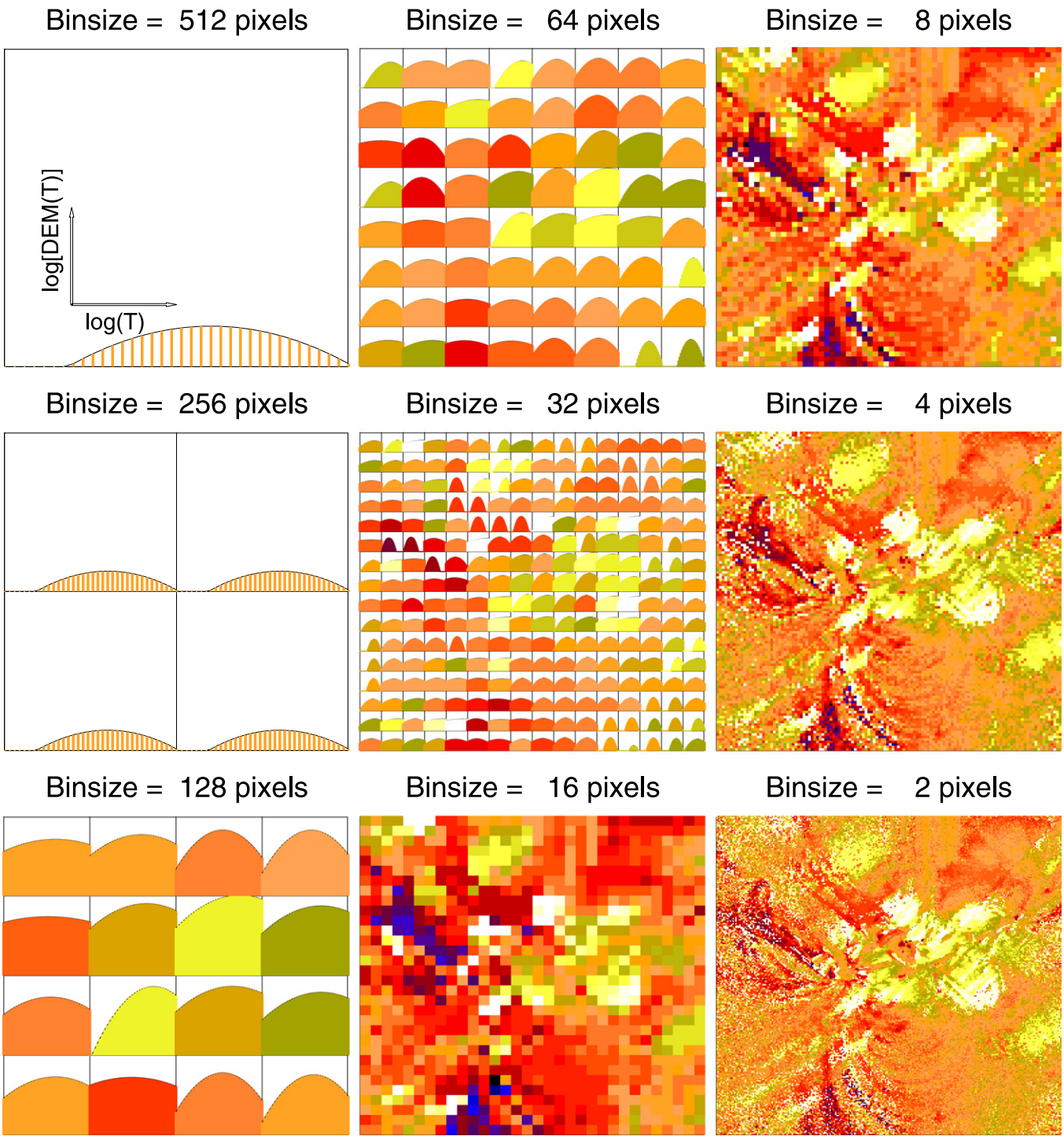

Figure 1. The spatial synthesis DEM method is visualized by single-Gaussian DEM fits in a grid $[x_i, y_j]$, $i = 1, \ldots, n_{\rm bin}$, $j = 1, \ldots, n_{\rm bin}$ of spatial positions with macropixels of bin size $\Delta x = 512/n_{\rm bin} = 512, 256, \ldots, 2$. Each macropixel shows a Gaussian DEM fit to the six coronal AIA wavelengths, covering a temperature range of $\log(T) = 5.8$–7.45 and emission measure range of $\mathrm{DEM}(T) = 10^{47}$–$10^{57}$ cm^{-5} K^{-1}. The colorscale is proportional to the logarithmic DEM peak temperature T_p, with blue at $T_p = 10^{5.8}$ K and white at $T = 10^{7.45}$ K. The data are obtained from event #12, a *GOES* X2.2-class flare observed with AIA on 2011 February 15, 01:40 UT.

the choice of a threshold, especially in flares that have a large dynamic range of fluxes over several orders of magnitude.

In order to eliminate the choice of wavelengths, we use the emission measure maps $\mathrm{DEM}_p(T; x, y, t)$ (Equation (7)), where we find a range of $\mathrm{DEM}_p = 8.2 \times 10^{22} - 2.7 \times 10^{25}$ cm^{-5} K^{-1} for the peak values. We choose an emission measure threshold near the lower bound of this range, i.e., $\mathrm{DEM}_{p,\rm min} = 10^{23}$ cm^{-5} K^{-1}, unless this threshold exceeds the 50% level of the peak emission measure, in which case we use the 50% level. This way, a flare area is always defined, even for flares with low emission measures. We measure then the flare area A of thermal emission by counting the number

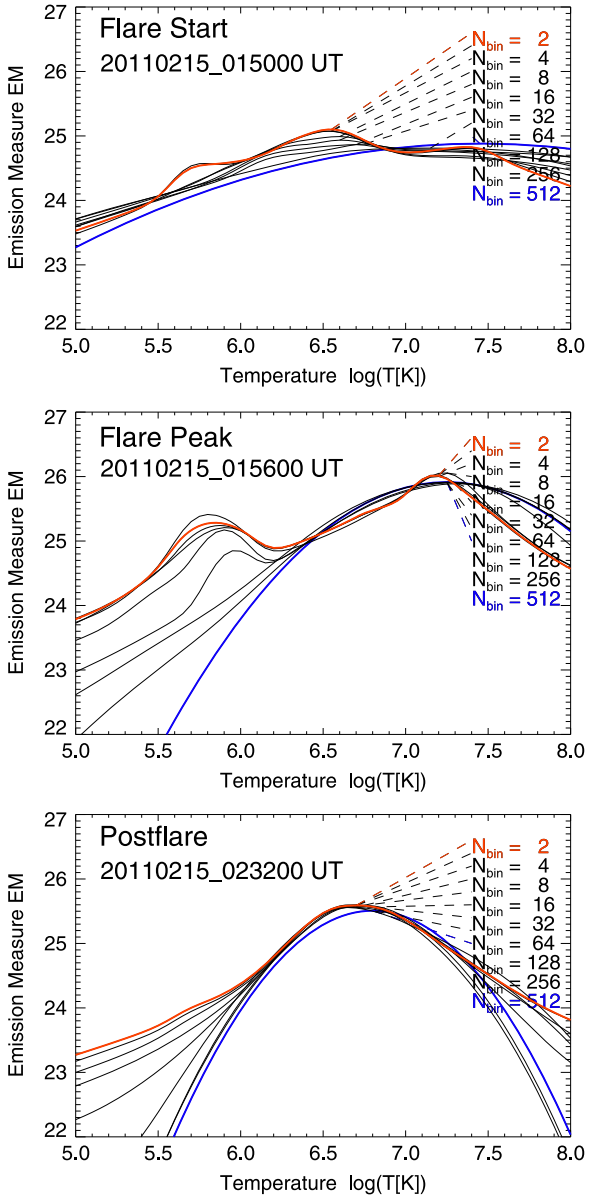

Figure 2. Spatial convergence of DEM distribution functions (from case shown in Figure 1), as a function of the macro-pixel size, from $N_{\rm bin} = 512$ (blue) to $N_{\rm bin} = 2$ (red), using the spatial synthesis DEM method, shown for three time steps during the 2011 February 15 flare, at flare start 01:50 UT (top panel), at flare peak 01:56 UT (middle panel), and in the postflare phase at 02:32 UT (bottom panel).

of macropixels above the threshold in an emission measure map $\mathrm{EM}_p(x, y)$, which multiplied with the macropixel size yields an area A (in units of cm^2), a length scale $L = A^{1/2}$, and a flare volume $V = L^3 = A^{3/2}$.

One problem that we encountered in our analysis is that the flare area at the peak time $t = t_p$ is sometimes largely inflated due to saturation of the EUV CCD, pixel bleeding, and diffraction patterns, and thus no reliable flare area A_i can be measured at the flare peak time t_i. Since the automated exposure control alternates between short and long exposure times during saturation, an over-exposed time frame (with flare area A_i at the peak time t_i) is interpolated from the preceding time step (with flare area A_{i-1} at time t_{i-1}) and the following time step (with flare area A_{i+1} at time t_{i+1}). In the derivation of geometric parameters in this study we use the maximum flare area $A = \max[A(t)]$ measured during the flare duration interval.

2.5. Multi-thermal Energy

If we substitute the expression of the total emission measure at the peak time t_p of the flare, $\mathrm{EM}_p = n_p^2 V$, into the expression for the thermal energy $E_{\rm th}$, we have the relationship

$$E_{\rm th}(t_p) = 3 n_p k_B T_p V = 3 k_B T_p \sqrt{\mathrm{EM}_p\, V}. \quad (11)$$

This expression is accurate only if the DEM function is a delta-function with a small thermal width w_T, which can then be characterized by the peak emission measure EM_p at the DEM peak temperature T_p.

For every broad temperature DEM distribution $\mathrm{DEM}(T)$, as it is the case for most solar flares, it is more accurate to perform the temperature integral (or summation over discrete temperature increments ΔT_k, which may be logarithmically binned). In the discretized form, the emission measure EM_k is integrated over the temperature interval ΔT_k is $\mathrm{EM}_k = \mathrm{DEM}(T_k)\Delta T_k$, and the thermal energy can be written as a summation of partial thermal energies from each temperature interval $[T_k, T_k + \Delta T_k]$ (see the Appendix),

$$E_{\rm th} = \sum_k 3 k_B V^{1/2} T_k\ \mathrm{EM}_k^{1/2} = 3 k_B V^{1/2} \sum_k T_k \left[\mathrm{DEM}(T_k)\ \Delta T_k\right]^{1/2}. \quad (12)$$

While the DEM peak temperatures T_p were determined within the parameter space of $T_p = 0.5-30$ MK, the temperature integral of the thermal energy (Equation (12)) was calculated in an extended range of $\log(T_e) = 5.0-8.0$, in order to fully include the Gaussian tails of the DEM fits in each macropixel. This yields a more accurate value of the total multithermal energy, since it avoids a truncation at the high-temperature tail of the composite DEM distribution. Note that we defined the thermal energy in terms of the volume-integrated total emission measure ($\mathrm{EM} = \int \mathrm{DEM}(T) dT = \int n_e^2 dV = n_e^2\ V$ (in units of cm^{-3}), in contrast to the column depth integrated emission measure per area, $\mathrm{EM}/A = \int \mathrm{DEM}(T)/A\ dT = \int n_e^2 dz = n_e^2 L$ (in units of cm^{-5}) used in the spatial synthesis method (Equation (7)), where the emission measure is quantified per unit area or per image pixel (see the detailed derivation in the Appendix). We find that the more accurate expression of Equation (12) typically yields a factor of $\approx$14 higher values for the thermal energies than the single-temperature approximation of Equation (11), and thus represents a very important correction for broad multi-temperature DEMs.

Considering the more complex DEM functions obtained from spatial synthesis with Equation (9), we will see that the DEM function often has multiple peaks, and thus it no longer makes any sense to talk about a single peak emission measure EM_p and single peak temperature T_p. In order to characterize such complex DEM functions with a characteristic temperature value, it makes more sense to define an emission measure-

weighted temperature T_w, which we define as,

$$T_w = \frac{\int T\ \mathrm{DEM}(T)dT}{\int \mathrm{DEM}(T)dT} = \frac{\sum_k T_k\ \mathrm{DEM}(T_k)\Delta T_k}{\mathrm{EM}}. \quad (13)$$

and approximately characterizes the "centroid" of the DEM function.

3. OBSERVATIONS AND RESULTS

3.1. AIA Observations

The dataset we are analyzing for this project on the global energetics of flares includes all M- and X-class flares observed with the *SDO* during the first 3.5 yr of the mission (2010 June 1 to 2014 January 31), which amounts to 399 flare events, as described in Paper I (Aschwanden et al. 2014a). The catalog of these flare events is available online, see http://www.lmsal.com/~aschwand/RHESSI/flare_energetics.html. We attempt to calculate the thermal energies in all 399 cataloged events, but we encountered eight events with incomplete or corrupted AIA data, so that we are left with 391 events suitable for thermal data analysis.

AIA provides EUV images from four 4096 × 4096 detectors with a pixel size of 0.″6, corresponding to an effective spatial resolution of ≈1.″6. We generally use a subimage with a FOV of FOV = 0.35 $R_\odot$. AIA records a full set of near-simultaneous images in each temperature filter with a fixed cadence of 12 s, while our analysis of the flare evolution is done in time increments of $\Delta t = 0.1$ hr. This cadence may underestimate the maximum thermal energy during a flare in some cases, but is estimated to be less than a factor of 2.

3.2. Example of DEM Analysis

An example of our DEM analysis is summarized in Figure 3, which applies to the first event (#1) of our list, a *GOES* M2.0 class flare in active region NOAA 11081 at N23 W47, observed with AIA/*SDO* on 2010 June 12, 00:00–01:30 UT. The *GOES* 1–8 Å light curve is shown in Figure 3(a), with *GOES* flare start time at t_s = 00:30 UT, peak time at t_p = 00:58 UT, and flare end time at t_e = 01:02 UT, according to the NOAA event list. The flare end time t_e is defined when the *GOES* flux drops down to 50% of the peak value, according to NOAA convention, but flare-related EUV emission always lasts significantly longer. In our thermal analysis we add margins of $\Delta t = 0.5$ hr before and after the NOAA flare start and end times, which covers the time interval of 00:00–01:32 UT in this event. We use a cadence of $dt = 0.1$ hr, which yields 14 time frames for this event. The six AIA flux profiles are shown in Figure 3(b), which show a very simple evolution of a single peak in all 6 EUV wavelengths, coincident with the SXR peak in *GOES* time profiles. The peak time occurs in time frame $i_t = 10$, at 00:58 UT. Flare background fluxes have been subtracted in every spatial macropixel (4 × 4 image pixels) separately (according to Equation (8)). Because every macropixel has a different background value $B_\lambda(x, y, t_b)$, the summation of all background subtracted profiles $F_\lambda(x, y, t) - B_\lambda(x, y, t)$ leaves residuals that amount to a fraction of ≈0.05–0.5 of the peak flux (see the preflare time profile of spatially-summed fluxes in Figure 3(b)).

For the DEM analysis we read 14 (time frames) times 6 (wavelength) AIA images, extract subimages within a FOV = 0.35 solar radii, which amount to a size of about 522 pixels, we rebin the images into 4 × 4 macropixels, yielding a spatial 2D array (x_i, y_j) of 130 × 130 macropixels, subtract in each macropixel a temporal minimum flux background, forward-fit a Gaussian DEM function in each macropixel, which yields the three Gaussian parameters: the DEM peak emission measure $\mathrm{EM}_p(x_i, y_j)$, DEM peak temperature $T_p(x_i, y_j)$, and thermal width $w_T(x_i, y_j)$, or a Gaussian DEM function $\mathrm{DEM}(T; x_i, y_j)$ (Equation (7)) for each macropixel. Summing the 130 × 130 = 16,900 single-Gaussian DEMs yields then a spatially synthesized DEM function that is shown in Figure 3(f) for each time step $i_t = 1, \ldots, 14$. The evolution of the DEM peak starts from a DEM peak temperature of $T_p(i_t = 1) = 10^{6.4} = 2.5$ MK and peaks at a value of $t_p(i_t = 10) = 10^{6.8} = 6.3$ MK, and decreases again to the preflare value. The evolution of this peak temperature $T_p(t)$ is also shown in Figure 3(c), along with the evolution of the mean temperature $T_e(t)$, the mean electron density $n_e(t) = \sqrt{\mathrm{EM}_p(t)/V}$, and the thermal energy $E_{\rm th}(t)$ (Equation (12)), in normalized units. The spatial distribution of the emission measure map $\mathrm{EM}_p(x_i, y_j)$ is shown in Figure 3(e), where instrumental diffraction patterns (diagonal features) and pixel bleeding (vertical feature) are visible also at the flare peak time. Since these instrumental effects are mostly a spatial re-distribution of photons inside the FOV of the observed image, we expect that they do not greatly affect the obtained DEM function after spatial integration. The emission measure maps serve to measure a wavelength-independent flare area A at the flare peak time (above some threshold; Section 2.4), which yields the equivalent length scale $L = A^{1/2}$. The physical parameters obtained for this event at the flare peak time are listed in Figure 3 (bottom right). Note that the peak temperature is only T_p = 6.31 MK, while the emission measure-weighted temperature T_w = 18.57 MK (Equation (13)) is substantially higher. The flare length scale (indicated with a square in Figure 3(e)) is L = 13.2 Mm, the electron density is $n_e = \sqrt{\mathrm{EM}_p/V} = 5.8 \times 10^{10}$ cm^{-3}, and the thermal energy is $E_{\rm th} = 7.0 \times 10^{30}$ erg for this event.

The goodness-of-fit or reduced χ^2-criterion of the DEM fit yields a mean and standard deviation of $\chi^2 = 0.24 \pm 0.43$ for the 14 DEM fits of this particular event #1 (Figure 3). As mentioned before (Section 2.2), the calculation of the reduced χ^2-criterion is based on the estimated uncertainty of the observed AIA fluxes, which is dominated by the incomplete knowledge of the instrumental response functions, estimated to be of order ≈10–25% (Testa et al. 2012; Boerner et al. 2014). Although the χ^2-value found for this particular event is relatively low, compared with the mean statistical expectation, it fits into the broad range of the obtained overall statistical distribution. In Figure 6(g) we plot the distribution of the χ^2 -values of the 391 fitted flare events, where the χ^2 value of each flare event is a time average, as well as a spatial average (using the spatial synthesis method). The peak of this distribution is near $\chi^2 \approx 1$ and the median is $\chi^2 \approx 1.3$ (Figure 6(g)), which indicates that the chosen model of the DEM parameterization (Equation (1)) yields a best fit that is consistent with the empirical estimates of uncertainties in the flux or response functions (Equation (6)). Of course, the Gaussian DEM parameterization, even when individually fitted in each pixel, may not always represent the best functional form of observed

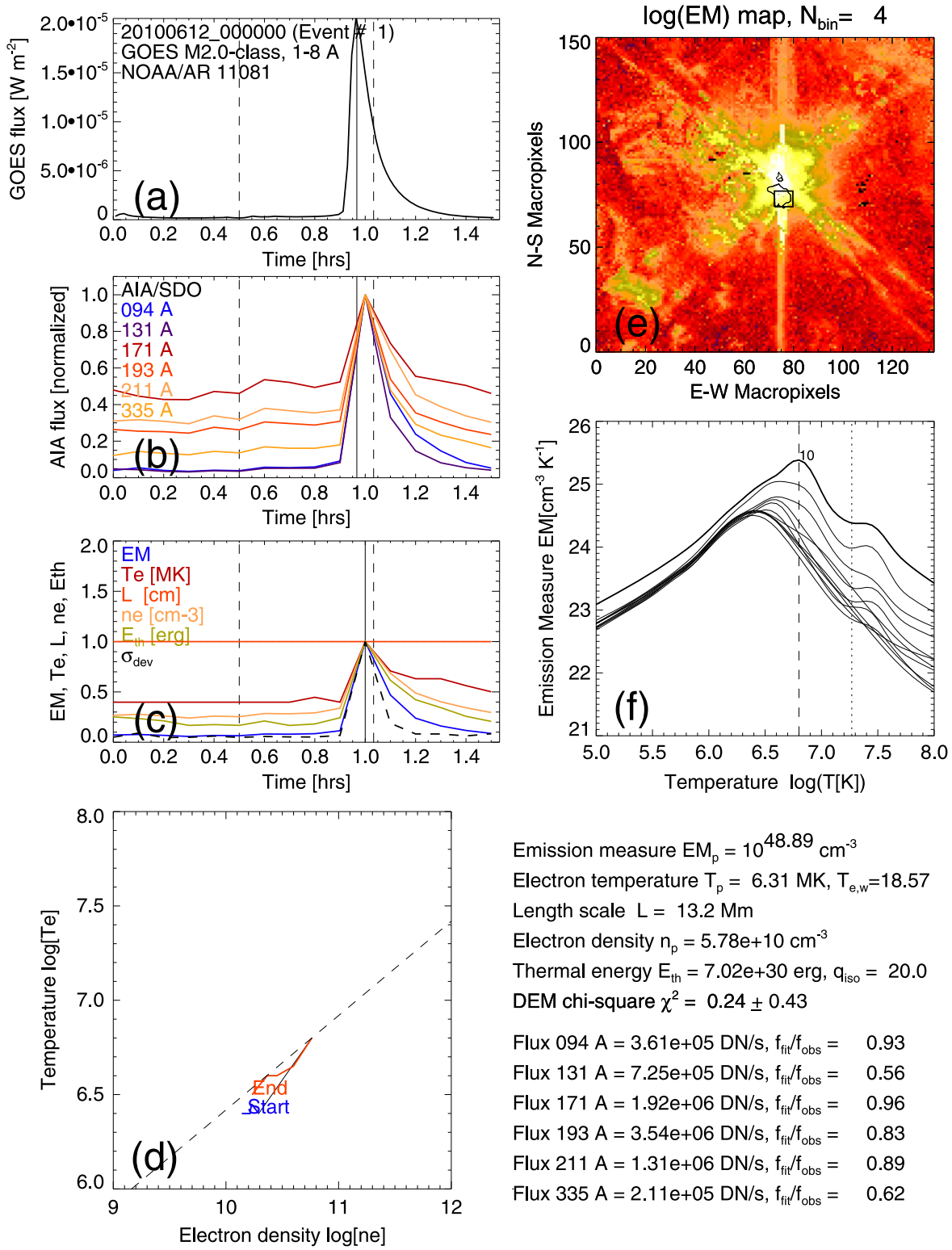

Figure 3. A summary of the DEM modeling of event #1, a *GOES* M2.0-class flare observed with AIA on 2010 June 12, 00:00 UT: (a) *GOES* 1–8 Å light curve with flare peak time (solid vertical line), start and end times (dashed vertical lines; (b) the background-subtracted light curves in the six coronal EUV channels from AIA/SDO (normalized to unity); (c) the evolution of physical parameters; (d) a $T_e - n_e$ phase diagram (with the RTV equilibrium indicated by a dashed line); (e) emission measure map EM(x, y) at the flare peak; (f) the spatial-synthesized DEM functions for all 14 time steps, with the emission measure maximum at time step 10; and the values of physical parameters at the flare peak time (bottom right).

DEMs, which may explain some χ^2-values significantly larger than unity. A more accurate goodness-of-fit test would require a more complex parameterization of the DEM function and a physical model of the flux uncertainties σ_λ, which should include systematic uncertainties due to the AIA flux calibration, the atomic (coronal and photospheric) abundances, the atomic transitions (computed with the CHIANTI code here), and the background subtraction method, which is not attempted here.

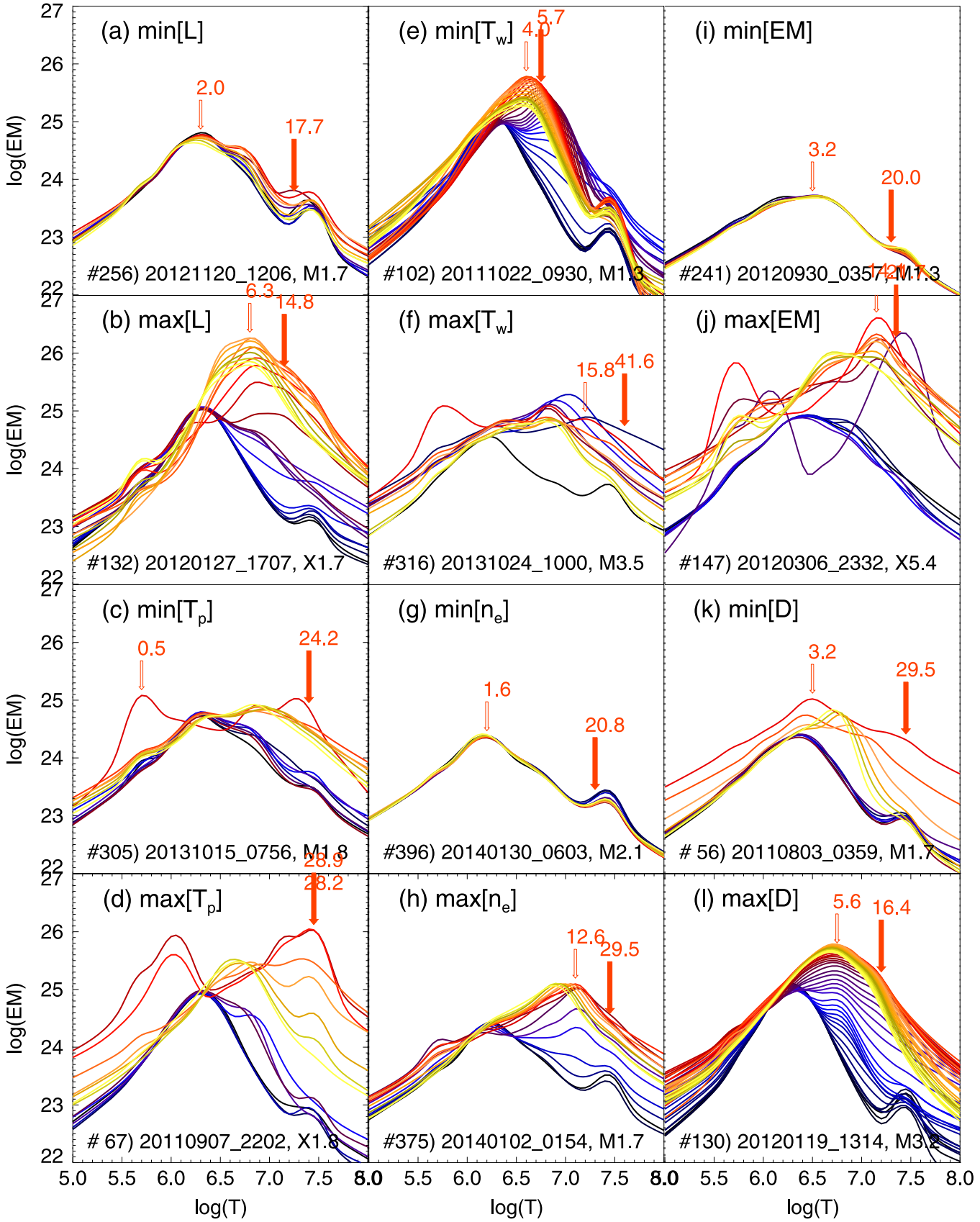

Figure 4. Differential emission measure distributions DEM(T) of 12 extremal flares, calculated with the spatial synthesis DEM method, are shown in evolutionary time steps of $dt = 0.1$ hr. The color scale indicates the transition from preflare (blue) to flare peak time (red) and postflare phase (yellow). The DEM peak temperatures T_p at the peak time t_p of the flare (red arrow) and the emission measure-weighted temperatures t_w (red solid arrow) are indicated in units of MK.

3.3. DEM Functions of Extreme Events

In Figure 4 we show the DEM distributions DEM(T) of 12 extreme events among the 391 analyzed M- and X-class flare events. These 12 events were selected by the minimum and maximum values in the parameters of the length scale L (Figures 4(a), (b)), the DEM peak temperature T_p (Figures 4(c), (d)), the emission measure-weighted temperature T_w (Figures 4(e), (f)), the electron density n_e (Figures 4(g), (h)), the DEM peak emission measure EM (Figures 4(i), (j)), and flare duration D (Figures 4(k), (l)). This selection of extreme events demonstrates the variety and diversity of DEM functions we encountered among the analyzed flare events. It shows also the versatility and adequacy of the DEM parameterization using spatially synthesized (single-Gaussian) DEM functions.

The length scales of thermal emission vary from $L_{\rm min} = 1.7$ Mm (#256; Figure 4(a)) to $L_{\rm max} = 45.9$ Mm (#132; Figure 4(b)). What is striking between the evolution of these two events is that the flare with the smallest size shows very little increase in the emission measure at any temperature, while the largest flare exhibits a large increase in the high-temperature emission measure.

For the peak temperatures we find a range from $T_p = 0.5$ MK (#305; Figure 4(c)) to $T_p = 28.1$ MK (#67; Figure 4(d)), which is not necessarily coincident with the emission measure-weighted temperature T_w. This is clearly shown in the case with the smallest peak temperature, which is far below the emission measure-weighted temperature of peaks in the DEM, which can make the peak temperature to jump around wildly as a function of time, as long as their associated DEM peak emission measures are comparable. This is a major reason why the DEM peak temperature should not be used in the estimate of thermal energies, but rather the emission measure-weighted temperature that is a more stable characteristic of the DEM function.

For the emission measure-weighted DEM function we find a range from $T_w = 5.7$ MK for the coldest flare (#102; Figure 4(e)) to $T_w = 41.6$ MK for the hottest flare (#316; Figure 4(f)), which is close to the upper limit of the temperature range where AIA is sensitive. The coldest flare in our selection with $T_w = 5.7$ MK is a M1.3 *GOES* class, while the hottest flare with $T_w = 41.6$ MK is a M3.5 *GOES* class. The *GOES* class does not necessarily correlate with the flare temperature, which is expected since the *GOES* class is mostly defined by the emission measures (in soft X-rays) rather than by the temperature.

For the electron density we find a range from $n_e = 10^{10.31}$ cm^{-3} (#396; Figure 4(g)) to $n_e = 10^{11.77}$ cm^{-3} (#375; Figure 4(h)), which corresponds to a variation by a factor of $\approx$30. The lowest density corresponds to a low peak temperature ($T_p = 1.6$ MK), while the highest density yields a high peak temperature temperature ($T_p = 29.5$ MK). For a fixed loop length, a correlation between the electron density and the electron temperature is expected according to the RTV scaling law, i.e., $n_p \propto T_p^2$ (Equation (21)).

For the DEM peak emission measure we find a variation from $\mathrm{EM}_p = 10^{47.31}$ cm^{-5} (#241; Figure 4(i)) to $\mathrm{EM}_p = 10^{50.26}$ cm^{-5} (#147; Figure 4(j)), which varies by a factor of $\approx$1000. The corresponding *GOES* classes are M1.3 and X5.4, which are both near the limits of the *GOES* class range (M1.0–X6.9) found in our selection. The event with the largest emission measure represents the second-largest *GOES* class (X5.4) in our selection, and thus the *GOES* class is indeed a good proxy to estimate the emission measure of flares.

The time range of flare durations is found to vary from $D = 0.1$ hr (#56; Figure 4(k)) to $D = 4.1$ hr (#130; Figure 4(l)). The longest duration event, however, does not have extreme values in temperature, emission measure, or length scale.

3.4. Statistics of Physical Parameters

We provide some statistics on the derived thermal parameters, such as the length scale L, the thermal volume V, the DEM peak temperature T_p, the emission measure-weighted temperature T_w, the electron density n_e, the total emission measure EM, and the thermal energy $E_{\rm th}$, in form of scatterplots (Figure 5) and size distributions (Figure 6). The inferred physical parameters are listed for the 28 X-class flares in Table 1, and for all 391 M- and X-class flares in the machine-readable Table 2. The ranges of these physical parameters have already been discussed in terms of extreme values in Section 3.3. The scatterplots shown in Figure 5 reveal us which parameters are correlated and indicate simplified scaling relationships, while the size distributions shown in Figure 6 reveal us the powerlaw tails that are typical for dissipative nonlinear systems governed by self-organized criticality (SOC).

The scatterplots shown in Figure 5 indicate that the thermal energy is correlated with the length scale L by the scaling relationship (Figure 5(a)),

$$E_{\rm th} \propto L^{2.3\pm0.1}, \tag{14}$$

and consequently is correlated with the volume V (Figure 5(b)) also,

$$E_{\rm th} \propto V^{0.76\pm0.04}, \tag{15}$$

and is correlated also with the total emission measure EM (Figure 5(f))

$$E_{\rm th} \propto \mathrm{EM}^{1.27\pm0.10}, \tag{16}$$

but strongly anti-correlated with the electron density n_e (Figure 5(e)), and is not correlated with the temperatures T_p (Figure 5(c)) and T_w (Figure 5(d)).

Regarding the size distributions, the *fractal-diffusive self-organized criticality (FD-SOC)* model provides predictions for the size distributions (Aschwanden 2012; Aschwanden et al. 2014b). The most fundamental parameter in the FD-SOC model is the length scale L, which according to the scale-free probability conjecture is expected to have a size distribution $N(L) \propto L^{-d}$ for Euclidean space dimension d. We find agreement between this theory and the data within the uncertainties of the fit (Figure 6(a)),

$$\alpha_L^{\rm obs} = 3.3 \pm 0.3, \qquad \alpha_L^{\rm theo} = 3.0. \tag{17}$$

For the volume V of thermal emission, the FD-SOC model predicts a powerlaw slope of $\alpha_V = 1 + (d-1)/d$, and we find good agreement (Figure 6(b)),

$$\alpha_V^{\rm obs} = 1.7 \pm 0.2, \qquad \alpha_V^{\rm theo} = 1.67. \tag{18}$$

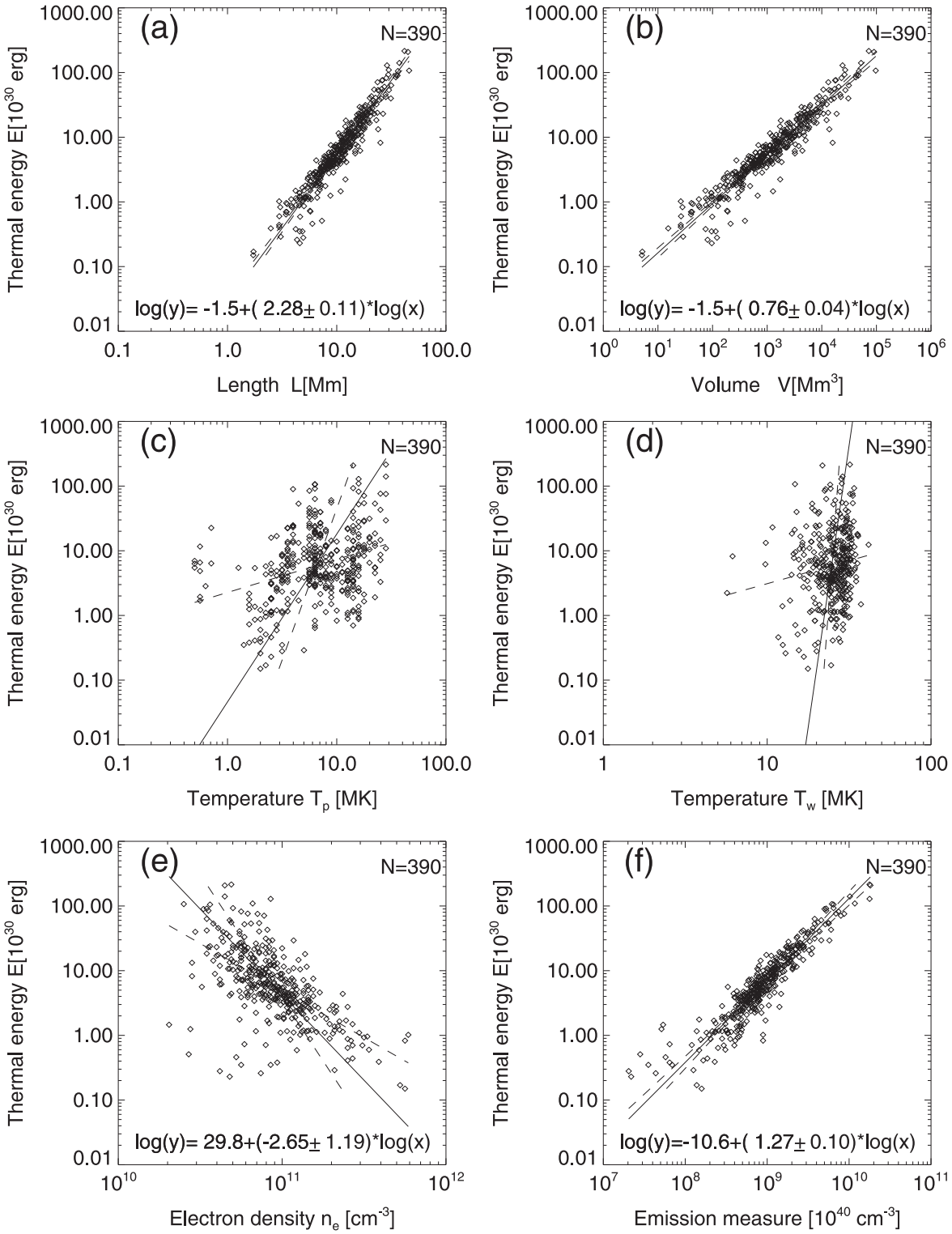

Figure 5. Scatter plot ot the thermal energy $E_{\rm th}$ as a function of physical parameters L, V, T_p, T_w, n_e, EM_p of the analyzed 391 M- and X-class flares. Linear regression fits (solid lines) are indicated with 1-σ uncertainties corresponding to the 67% confidence level (dashed lines).

For the energy E, using the observed scaling, i.e., $E_{\rm th} \propto V^{\gamma}$ with $\gamma = 0.76$ (Equation (15)), we expect then a size distribution of

$$N\left(E_{\rm th}\right)dE_{\rm th} \propto N\left[V\left(E_{\rm th}\right)\right]\left|dV/dE_{\rm th}\right|dE_{\rm th} \propto E_{\rm th}^{-(1+(2/3)\gamma)},$$

which predicts a powerlaw slope of $\alpha_{E\rm th} = [1 + (2/3)\gamma] \approx 1.88$,which is indeed consistent with the observed slope,

$$\alpha_E^{\rm obs} = 1.8 \pm 0.2, \qquad \alpha_E^{\rm theo} = 1.88. \tag{19}$$

We have to keep in mind that the FD-SOC model is a very generic statistical model that predicts a universal scaling law for spatial parameters, based on the scale-free probability

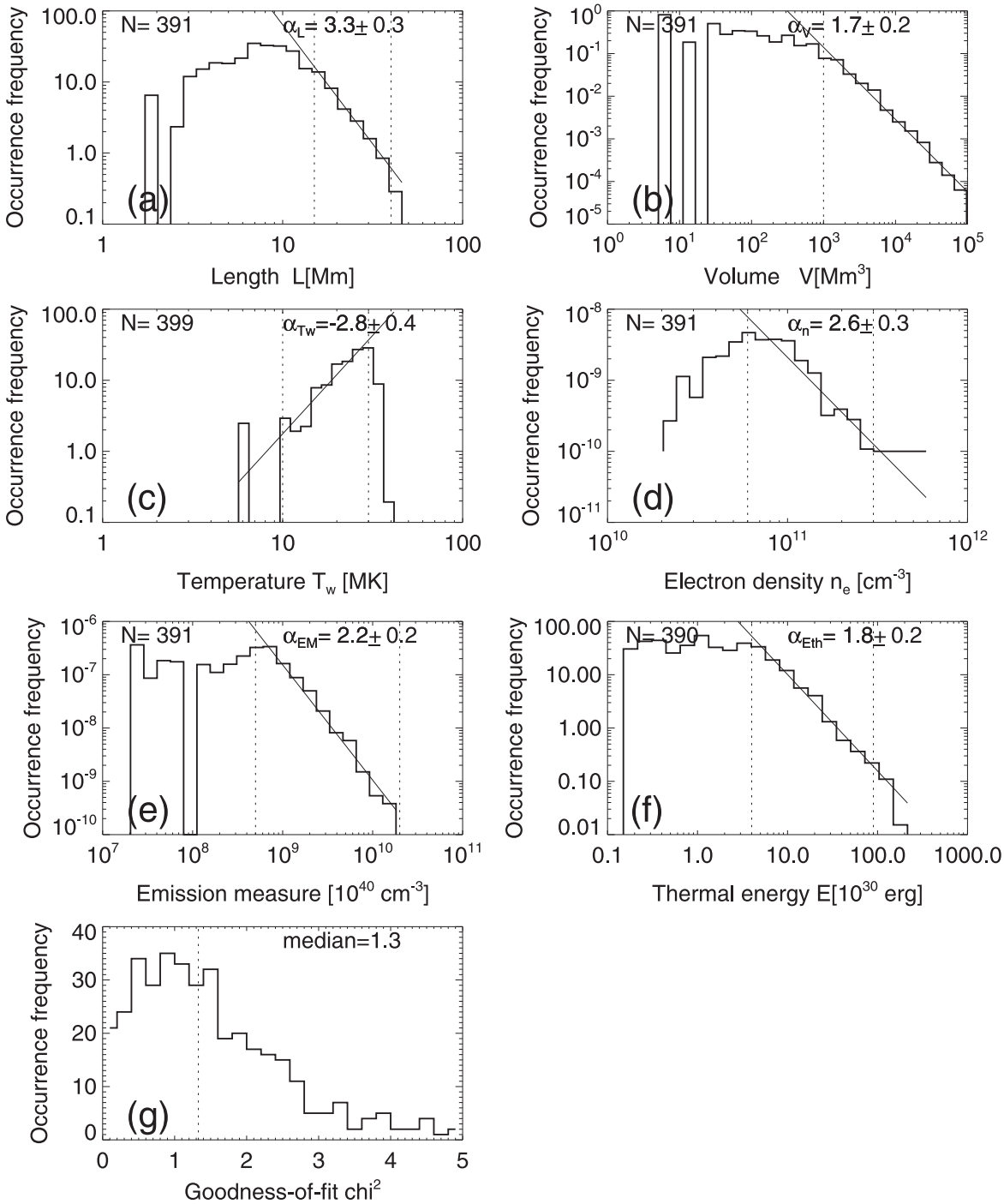

Figure 6. Size distributions of the physical parameters L, V, T_w, n_e, EM and $E_{\rm th}$ for the 391 analyzed M- and X-class flares. A powerlaw function is fitted in the range indicated with dotted vertical lines. The reduced χ^2 distribution peaks near 1.0 and has a median of 1.3.

conjecture, i.e., $N(L) \propto L^{-d}$ (Aschwanden 2012), while the scaling of other physical parameters, such as the energy, $E_{\rm th} \propto V^{\gamma}$, requires a physical model that is specific to each SOC phenomenon. In the next section we will discuss the Rosner–Tucker–Vaiana (RTV) scaling law, which we apply to model the otherwise unknown scaling of the energy with the volume, $E_{\rm th} \propto V^{\gamma}$.

3.5. The Rosner–Tucker–Vaiana Scaling Law

A well-known physical scaling law between hydrodynamic parameters of a coronal loop is the Rosner–Tucker–Vaiana law (Rosner et al. 1978), which is derived under the assumption of energy balance between the energy input by a volumetric heating rate E_h (in units of erg cm^{-2} s^{-1}) and the radiative E_R and the conductive loss rates E_C, i.e., $E_H - E_R - E_C = 0$, which yields two scaling laws between the loop length L, loop apex electron temperature T_e, average electron density n_e, and heating rate E_H. While this original derivation applies to a steady-state of a heated coronal loop, it turned out that the same scaling laws apply also to solar flares at the heating/cooling turnover point (Aschwanden & Tsiklauri 2009). Solar flares are generally not heated under steady-state conditions, except at the turning point of maximum temperature, when the heating rate

and the radiative and conductive losses are balanced for a short instant of time. Before reaching this turning point, heating dominates the cooling losses, while the cooling dominates after this turning point.

We can express the RTV scaling laws explicitly for the parameters T_e, n_e, L, EM, $E_{\rm th}$ (Aschwanden & Shimizu 2013),

$$T_{\rm RTV} = c_1\, n_e^{1/2}\, L^{1/2}, \qquad c_1 = 1.1 \times 10^{-3}, \tag{20}$$

$$n_{\rm RTV} = c_2\, T_e^2 L^{-1}, \qquad c_2 = 8.4 \times 10^{5}, \tag{21}$$

$$L_{\rm RTV} = c_3\, T_e^2 n_e^{-1}, \qquad c_3 = 8.4 \times 10^{5}. \tag{22}$$

$$\mathrm{EM}_{\rm RTV} = \int n_e^2\, dV = n_e^2 V = n_e^2 \left(\tfrac{2\pi}{3} L^3\right) = c_4\, T_e^4 L, \quad c_4 = 1.48 \times 10^{12}. \tag{23}$$

$$E_{\rm th,RTV} = 3 n_e k_B T_e V = c_5\, T_e^3 L^2, \qquad c_5 = 7.3 \times 10^{-10}. \tag{24}$$

We can then compare the observed parameters T_e, n_e, L, EM, $E_{\rm th}$ with these theoretically predicted parameters $T_{\rm RTV}$, $n_{\rm RTV}$, $L_{\rm RTV}$, $\mathrm{EM}_{\rm RTV}$, $E_{\rm th,RTV}$, which is shown in Figure 7. Note that we use the weighted temperature T_w and the emission measure EM_p and density n_p measured at the peak time t_p of the flare here. While the original RTV scaling law has no free parameters, the scaling between the average loop half length $L_{\rm loop}$ (required for the RTV scaling law) and the average length scale L (measured here during the flare duration) requires a geometric model, as well as information on filling factors and fractal geometry. Since detailed modeling of the 3D geometry of flare loop configurations is beyond the scope of this study, we determine the average scaling ratio empirically and find that a relationship of $L \approx (2\pi)\, L_{\rm loop}$ yields a satisfactory match between the observed and the theoretically predicted physical parameters of the RTV scaling law (indicated with the dotted diagonal line expected for equivalence in Figure 7).

We see now that the three-parameter RTV scaling laws (Figure 7) retrieve the relationships obtained from 2-parameter correlations (Figure 5). The correlation of the thermal energy with length scale, $E_{\rm th} \propto L^{2.3\pm0.1}$ (Equation (14); Figure 5(a)) is similar to the RTV relationship $E_{\rm th} \propto L^2$ (Equation 24), which is equivalent to the relationship with the volume, i.e., $E_{\rm th} \propto V^{0.76\pm0.04}$ (Equation (15); Figure 5(b)) and the RTV relationship $E_{\rm th} \propto L^2 \propto V^{2/3}$ (Equation (24)). Combining the RTV relationships between $E_{\rm th}$ (Equation (24)) and EM (Equation (23)) we obtain $E_{\rm th} \propto \mathrm{EM}_p(L/T)$, which is *similar* to the observed two-parameter correlation $E_{\rm th} \propto \mathrm{EM}^{1.3\pm0.1}$. Thus the two-parameter correlations are approximations of the three-parameter (RTV) scaling laws, and thus can be explained by a physical model, although they are less accurate because of the neglected third parameter. Comparing the observed and RTV-predicted values (as shown in Figure 7), we find that the (multi-)thermal energies $E_{\rm th,RTV}$, emission measures $\mathrm{EM}_{\rm RTV}$, and length scales $L_{\rm RTV}$ are correlated with the observed values within a standard deviation, while the temperature $T_{\rm RTV}$ and density $n_{\rm RTV}$ deviate more than a standard deviation, which is likely to be caused by their smaller ranges of values and the associated truncation effects (e.g., see calculation of truncation effects in Figure 8 of Aschwanden & Shimizu 2013).

3.6. Comparison of Magnetic and Thermal Energies

The main goal of the global flare energetics project is the comparison and partitioning of various flare energies. In Paper I we calculated the dissipated magnetic energies in 172 M- and X-class flares, based on the (cumulative) decrease of free energies during each flare, which were found to have a range of $E_{\rm diss} = (1.5\text{–}1500) \times 10^{30}$ erg. In this study we calculated the thermal energy at the peak time of the total emission measure and find a range of $E_{\rm th} = (0.15\text{–}315) \times 10^{30}$ erg. A scatterplot between the magnetic and thermal energies is shown in Figure 8(a). From this diagram we see that the average ratio is $E_{\rm th}/E_{\rm diss} \approx 0.082$, with a standard deviation by a factor of 4.8, which defines a typical range of $E_{\rm th}/E_{\rm diss} = 0.02\text{–}0.40$. Thus, the thermal energy amounts generally only to a fraction of ≈2–40% of the dissipated magnetic energy, as determined with the coronal NLFFF method.

We show also a scatterplot of the thermal energy with the dissipated magnetic energy as computed with the photospheric NLFFF method, which could be performed only for 12 events (Figure 8(b)). In this samll dataset, the average ratio is $q_e = 0.76$, with a scatter by a factor of 6.5, or a range of $q_e \approx$ 0.12–4.8. In four out of the 12 events the thermal energy exceeds the dissipated magnetic energy, which is likely to be a false result due to underestimates of the dissipated magnetic energy, since the PHOT-NLFFF code seems to be less sensitive in measuring decreases of the free energy than the COR-NLFFF code, possibly due to a smoothing effect caused by the preprocessing procedure.

We compare the new results also with the previous study by Emslie et al. (2012), where the thermal energy could be determined for 32 large eruptive flares, while the magnetically dissipated energy was estimated to be 30% of the potential energy. In that study, the average ratio of the thermal to the magnetically dissipated energy is found to be $E_{\rm th}/E_{\rm diss} \approx 0.0045$ with a scatter by a factor of ≈2.3, which yields a range of 0.2–1.0% (Figure 8(c)). Since the thermal energies have a similar median value ($E_{\rm th,med} = 4.6 \times 10^{30}$ erg) as we find in this study ($E_{\rm th,med} = 6.0 \times 10^{30}$ erg), the discrepancy is most likely attributed to an overestimate of the magnetically dissipated energies, as well as to a selection effect of larger flares. The median value of the magnetically dissipated energy is $E_{\rm diss,med} = 1300 \times 10^{30}$ erg in Emslie et al. (2012), while we find a median value of $E_{\rm diss,med} = 110 \times 10^{30}$ erg, which is about an order of magnitude lower, and goes along with our finding that the free energy is about 1–25% of the potential free energy, rather than 30% as assumed in the study of Emslie et al. (2012).

4. DISCUSSION

4.1. Previous Measurements of Thermal Flare Energies

Most previous studies estimated thermal flare energies by using the isothermal relationship, i.e., $E_{\rm th} = 3 k_B T_p \sqrt{\mathrm{EM}_p\, V}$, which requires a DEM analysis (to obtain the peak emission measure EM_p and peak temperature T_p) and imaging observations (in order to obtain the flare area or volume V), measured at the flare peak time. A DEM analysis requires multiple temperature filters, and thus thermal flare energies can only be obtained from instruments with multi-wavelength imaging capabilities. Statistics of thermal energies was gathered for large flares, nanoflares, and impulsive brightenings in EUV and

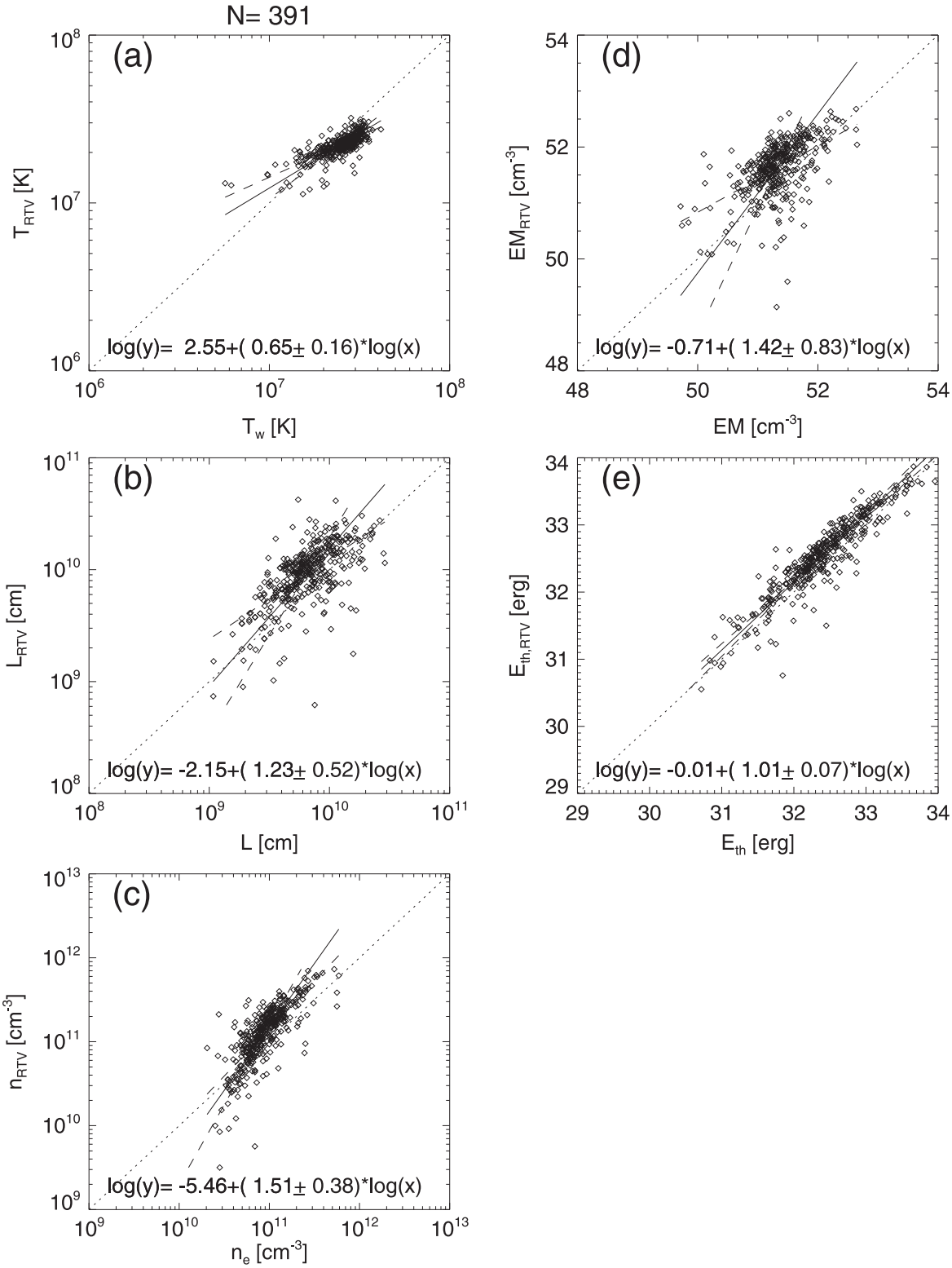

Figure 7. Observed (x-axis) and predicted physical parameters (y-axis) based on the Rosner–Tucker–Vaiana model. Linear regression fits (solid lines) and uncertainties (dashed lines) are indicated, along with the line for equivalence (dotted line).

soft X-rays from *Skylab S-054* (Pallavicini et al. 1977), *Yohkoh/SXT* (Aschwanden & Benz 1997; Shimizu 1997; Shimojo & Shibata 2000), SoHO/EIT (Krucker & Benz 2000); TRACE (Aschwanden et al. 2000; Aschwanden & Parnell 2002), *RHESSI* (Emslie et al. 2004, 2005, 2012; Caspi et al. 2014), and AIA/*SDO* (Aschwanden & Shimizu 2013).

How consistent are the thermal energies determined here with previous measurements? We compile some statistics on thermal energy measurements in large flares in Table 3, by listing the instruments, the number of events, and the parameter ranges of the spatial scale L, the peak electron temperature T_p, the peak electron density n_p, the peak emission measure EM_p,

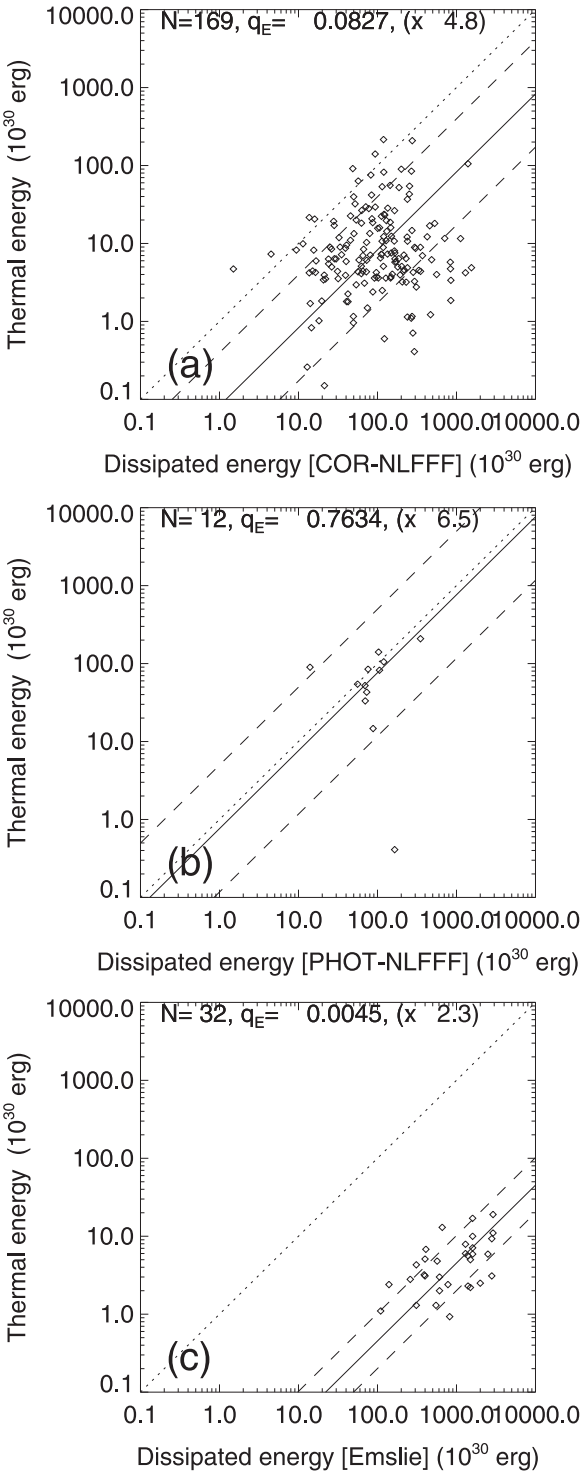

Figure 8. Scatterplot of thermal energies E_{th} vs. magnetically dissipated energies E_{diss}: (a) The 172 M- and X-class flares from which the magnetically dissipated energy was determined in Paper I (Aschwanden et al. 2014) with the COR-NLFFF method; (b) 12 events with magnetic energies calculated with the PHOT-NLFFF method; (c) 32 large eruptive flares from Emslie et al. (2012). The mean ratio q_E (solid line) and standard deviations (dashed lines, expressed by a multiplication factor ×) are indicated, along with the line for equivalence (dotted line).

and the thermal energy E_{th}. A scatterplot of thermal energies $E_{th}(V)$ versus the flare volumes V measured in large flares is shown in Figure 9. In particular, statistics on large flares (approximately *GOES* M- and X-class) has been analyzed in 31 events from *Skylab* S-054 (Pallavicini et al. 1977), in 32 events from *RHESSI* (Emslie et al. 2012), in 155 events from AIA/*SDO* (Aschwanden & Shimizu 2013), and in 391 events from AIA/*SDO* in the present study. Table 3 provides the ranges of reported physical parameters, but we have to be aware that different event selections have been used in the different datasets.

4.2. Isothermal Versus Multi-thermal Energies

The most striking discrepancy appears between the isothermal and multithermal energies, which is measured for the first time in this study. We overlay the thermal energies E_{th} as a function of the flare volume V for the same four studies in Figure 9. In the present study we calculate both the isothermal energy $E_{th,iso}$ (Equation (11)) and the multithermal energy $E_{th,multi}$ (Equation (12)) and find a systematic difference of $E_{th,multi}/E_{th,iso} \approx 14$ (Figures 9, 10). Note the offset of the linear regression fits between isothermal energies (black line and diamonds in Figure 9) and multithermal energies (orange line and diamonds in Figure 9). The multithermal flare energy definition has to our knowledge not been applied in the calculation of thermal flare energies in all previous studies, but is very important, because it boosts the thermal energy produced in flares statistically by an average factor of ≈14, as measured from the energy offset in cumulative size distributions (Figure 10). This is related to the incompatibility of iso-thermal temperatures inferred from *GOES*, AIA, and *RHESSI* data, investigated in a recent study (Ryan et al. 2014), which can only be ameliorated with broadband (multi-temperature) DEM distributions. The systematic underestimate of the thermal energy, when the isothermal approximation is used, may also be the reason why a very low value of $E_{th}/E_{diss} = 0.2$–1% (Figure 8(c)) was found for the thermal/magnetic energy ratio in Emslie et al. (2012), compared with our range of $E_{th}/E_{diss} = 2$–40% (Figure 8(a)) calculated in the present study.

4.3. Flare Volume Measurements

The thermal energy depends on the volume V, and thus the measurement of flare areas or volumes are crucial to obtain an accurate energy value. Since we can directly observe in 2D images the flare area A only, the definition of a flare volume V is subject to modeling. The simplest definition is the Euclidean relationship $V = A^{3/2}$ and $L = A^{1/2}$, but more complicated definitions involve the fractal dimension (Aschwanden & Aschwanden 2008a, 2008b), 3D filling factors (Aschwanden & Aschwanden 2008b), or other geometric concepts to characterize the inhomogeneity of flare plasmas. One prominent modeling concept is the hydrostatic density scale height $\lambda(T)$, which depends on the flare plasma temperature T and can be used to estimate the vertical height above the solar surface. The detailed geometry of the flare plasma often appears to have the geometry of an arcade of loops, which can be highly inhomogeneous, depending on the spatial intermittency of precipitating electrons along the flare ribbons. Nevertheless, regardless how complicated the spatial topology of a flare is, the thermal energy is a volume integral and thus should be rotation-invariant to the aspect angle or heliographic location (assuming that we measure correct DEMs along each line-of-sight). This argument justifies isotropic geometries such as hemispheric flare volumes (Aschwanden & Shimizu 2013),

Table 3
Parameter Ranges of Physical Parameters Determined from Four Different Datasets of Large Flares

Instrument	Number of Events n	Spatial Scale $\log(L)$ (Mm)	Electron Temperature $\log(T_w)$ (MK)	Electron Density $\log(n_e)$ (cm^{-3})	Emission Measure $\log(EM_p)$ (cm^{-3})	Thermal Energy $\log(E_{th})$ (erg)
Skylab/S-054[a]	31	8.7–9.7	6.8–7.1	9.9–11.3	40.1–49.3	28.6–31.0
RHESSI[b]	32					30.0–31.3
AIA/*SDO*[c]	155	8.6–9.8	6.1–7.3	9.6–11.9	47.0–50.6	28.3–32.0
AIA/*SDO*[d]	391	8.2–9.7	5.7–7.4	10.3–11.8	47.3–50.3	28.3–31.7
AIA/*SDO*[e]	391	8.2–9.7	6.8–7.6	10.3–11.8	47.3–50.3	28.3–32.0

[a] Pallavicini et al. (1977).
[b] Emslie et al. (2012).
[c] Aschwanden & Shimizu (2013).
[d] This Study: Isothermal Energy.
[e] This Study: Multithermal Energy.

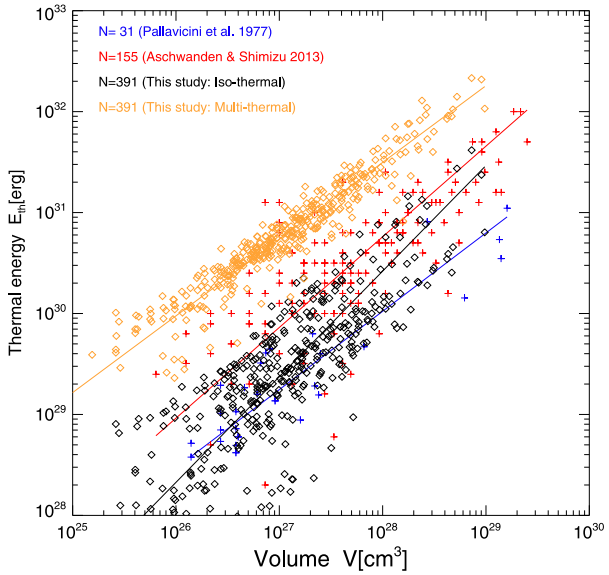

Figure 9. Comparison of thermal energies as a function of the flare volume size for four sets of measurements: Pallavicini et al. (1977) (blue crosses), Aschwanden & Shimizu (2013) (red crosses), isothermal energy in this study (black diamonds), and multithermal energy in this study (orange diamonds). Note that the multithermal energies are about an order of magnitude higher than the isothermal energies.

or the related Euclidean relationship $V \approx L^3$. Moreover, the height $h = L/2$ of semi-circular flare loops is about half of the footpoint separation L, and thus the volume $V = L^2h = (L^3)/2$ can be approximated with a cube $V \approx L^3$. Hence, we use the simple Euclidean relationships $V = A^{3/2}$ and $L = A^{1/2}$ in this paper. Detailed geometric 3D modeling of the flare volume at different temperatures is beyond the scope of this study.

How consistent is the flare volume measurement in the present work with previous studies? Most flare area measurements are done using a flux threshold, which is chosen above the data noise level and lower than the maximum flux in an image, but is arbitrary within this range. The volume of limb flares from Skylab data (Pallavicini et al. 1977) was calculated from measuring the height and size of bright soft X-ray emission in photographs and yields a remarkable good match for the isothermal energy with our present study (blue line and crosses in Figure 9). The previous study of 155 M- and X-class flares with AIA/*SDO* data (Aschwanden & Shimizu 2013) involved multiple flux threshold levels and was combined from six different wavelength filters, but is consistent with the area measurements in this study within a factor of $\lesssim 2$. This uncertainty translates into a factor of $2^{3/2} \approx 3$ for volumes, total emission measures, and thermal energies.

4.4. Spatial-synthesized DEM Analysis

DEM analysis is a prerequisite tool for determining thermal energies. The thermal width of the DEM distribution is the most crucial parameter to discriminate between isothermal and multithermal cases. Numerical integrations of the DEM temperature distribution show that multithermal DEMs yield in the average 14 times higher (multi-)thermal energies than isothermal (delta-function-like) DEM distributions (Figure 10). Thus, the fidelity of the DEM reconstruction is important for the accurate determination of thermal flare energies.

In this study we employed the spatial synthesis DEM method (Section 2.3 and Aschwanden et al. 2013), which approximates the DEM in every (macro-)pixel with a three-parameter Gaussian DEM function, which is then synthesized for the entire flare volume by adding all partial DEM distributions from each pixel. In Figure 2 we demonstrated that this method converges to a unique DEM solution by iterating from large macro-pixels to smaller sizes, down to a single image pixel. We find that this method converges rapidly, when iterating macro-pixel sizes $\Delta x = X \times 2^{-i}$, $i = 0, \ldots, 8$, on an image with full size X (Figures 1 and 2). This means that macropixels with a size of a few pixels isolate hot flare areas and ambient cooler plasma areas sufficiently to be characterized with a single-peaked DEM function. The fast convergence to a unique DEM function is very fortunate and relieves us from more sophisticated DEM modeling.

We find that the largest uncertainty in DEM modeling comes from uncertainties of the instrumental response functions, including missing atomic lines, chemical abundance variations, and preflare-background subtraction, which all combined are estimated to be of order ≈10–25% (Testa et al. 2012; Boerner et al. 2014; M. J. Aschwanden et al. 2015, in preparation), which is also confirmed from DEM inversions applied to synthetic data generated with 3D MHD simulations (Testa et al. 2012).

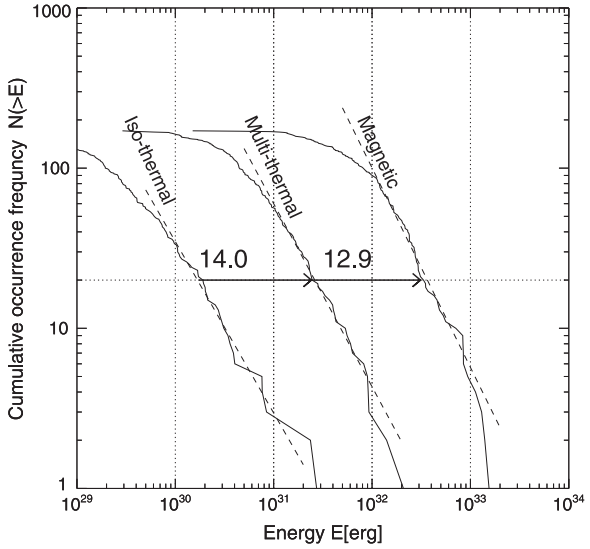

Figure 10. Cumulative occurrence frequency distributions of isothermal, multithermal, and dissipated magnetic energies in 171 M- and X-class flares. Note that the energy values have a characteristic ratio of $E_{\rm th,multi}/E_{\rm th,iso} \approx 14$ and $E_{\rm magn}/E_{\rm th,multi} \approx 12.9$.

4.5. Scaling Law and Extreme Events

In Section 3.5 we derived a physical scaling law for the thermal energy, $E_{\rm th,RTV} = 7.3 \times 10^{-10}\, T_p^3 L_p^2$ (Equation (24)), based on the RTV scaling law of 1D hydrostatic loops that are in steady-state energy balance between heating and cooling processes. The observational measurements of (multithermal) energies were found indeed to match this predicted relationship closely (see correlation between theoretically predicted and observed thermal energies in Figure 7(e)).

Let us consider the parameters of the most extreme events. For the largest flare in our dataset, we found a length scale of $L_p = 10^{9.7} \approx 50$ Mm ≈ 0.07 solar radius, the hottest flare has an (emission measure-weighted) temperature of $T_p = 10^{7.6} \approx 40$ MK, and the most energetic flare has a multithermal energy of $E_{\rm th} = 10^{32.0}$ erg. The upper limit for thermal energies is of particular interest for predictions of the most extreme (and worst events for space weather and astronauts). Based on the largest flare events observed in history, with a *GOES*-class of X10 to X17, an even larger maximum flare energy of $E_{\rm max} \approx 10^{33}$ erg was estimated, while stellar flares may range up to $E_{\rm max} \approx 10^{36}$ erg (see Figure 3 in Schrijver et al. 2012).

On the other extreme, the RTV scaling law (Equation (24)) may also be applied to predict the magnitude of the smallest coronal flare events. An absolute lower limit of flare temperatures is the temperature of the ambient solar corona, which is approximately $T_{\rm min} \approx 1.0$ MK. For a lower limit of the spatial size of a flare event we can use the size of the smallest loop that sticks out of the chromosphere, which has a height of $h_{\rm chrom} \approx 2$ Mm and a semi-circular loop length of $L_{\rm min} = \pi h_{\rm chrom} \approx 6$ Mm. The apex segment that sticks out of the chromosphere can have a projected length scale as short as $L_{\rm min} \gtrsim 1$ Mm. The extrapolated thermal energy of the smallest flare is then estimated to be $E_{\rm th} = 7.3 \times 10^{-10}\, T_{\rm min}^3 L_{\rm min}^2 \approx 7 \times 10^{24}$ erg, which is about nine orders of magnitude smaller than the largest flare, and thus called a nanoflare. This is consistent with the smallest observed nanoflares, which have been found to have a thermal energy of $E_{\rm th} \approx 10^{24} - 10^{26}$ erg (Aschwanden et al. 2000; Krucker & Benz 2000; Parnell & Jupp 2000; Aschwanden & Parnell 2002). Note that these predictions are based on our calculations of the multithermal energy, which amounts to an average correction factor of $\lesssim$14.

4.6. Self-organized Criticality Models

The statistics of nonlinear dissipative events often follows a scale-free powerlaw distribution, in contrast to (linear) random processes (such as photon statistics of a steady source), which follow a Poisson distribution (or its exponential approximation). The powerlaw function in occurrence frequency distributions (or size distributions) has been declared as a hallmark of nonlinear systems governed by SOC (Bak et al. 1987). A quantitative derivation of the powerlaw distribution function of SOC processes has been derived in the framework of the fractal-diffusive SOC model (FD-SOC: Aschwanden 2012; Aschwanden et al. 2014b), which predicts universal values for the powerlaw slopes of spatio-temporal parameters, based on the *scale-free probability conjecture*, $N(L) \propto L^{-d}$, the fractal geometry of nonlinear dissipative avalanches, and diffusive transport of the avalanche evolution. We measured the size distributions of spatio-temporal physical parameters in solar flares (length L, area A, volume V, durations D) and found indeed agreement with the predictions of the standard FD-SOC model (Figure 6). The size distributions of the other physical parameters (T_p, n_p, EM$_p$, $E_{\rm th}$), however, are not universal, but depend on the underlying physical process of the SOC phenomenon. For solar flares in particular, we found that the RTV scaling law is consistent with the observed parameter correlations and size distributions. Most of the physical scaling laws are expressed in terms of powerlaw exponents (such as the thermal energy, i.e., $E_{\rm th} \propto T_p^3 L_p^2$), which has the consequence that all size distributions of physical parameters are also predicted to have a powerlaw shape, except for finite-size effects (that produce a steep drop-off at the upper end) and incomplete sampling due to limited sensitivity (which produces a turnover at the lower end), as manifested in the size distributions shown in Figure 6. What the observed size distributions show, is the scale-free parameter range (also called inertial range) of SOC processes over which an identical physical process governs nonlinear energy dissipation. The size distributions shown in Figure 6 exhibit no indication of multiple or broken powerlaws in the inertial range of M- and X-class flares. Note that such powerlaw distributions occur only for statistically complete samples (above some threshold value). Datasets with "hand-selected" events (such as the 37 eruptive flare events sampled in Emslie et al. 2012) do not exhibit powerlaw-like size distributions.

Various flare energy size distributions have been compared in previous studies (e.g., see composite size distribution in Figure 10 of Aschwanden et al. 2000, based on size distributions published by Crosby et al. 1993; Shimizu 1997; Aschwanden et al. 2000; Krucker & Benz 2000; and Parnell & Jupp 2000). Such composite size distributions have been used to characterize the overall size distributions from the smallest nanoflare to the largest X-class flare. However, the construction of a synthesized flare energy size distribution requires a consistent definition of energy, which is not the case in most of the published studies, since they contain thermal as well as nonthermal energies. In order to illustrate this discrepancy we

show the cumulative size distributions of isothermal, multithermal, and magnetic flare energies in Figure 10, where we sample an identical event list, which is the common subset of the three energy forms and contains 171 events. In Figure 10 we show a cumulative size distribution of these events, constructed with the inverse rank-order plot. Note that the three different forms of energy differ by an approximate amount of $(E_{\rm magn}/E_{\rm th,multi}) \approx 13$ and $(E_{\rm th,multi}/E_{\rm th,iso}) \approx 14$. It is therefore imperative to derive the same form of energy when comparing the occurrence probabilities from the size distributions of different datasets.

4.7. Thermal/Magnetic Energy Ratios

One key result of this study is the thermal/magnetic energy ratio, for which we found a range of $E_{\rm th}/E_{\rm diss} \approx 2 - 40\%$. We consider this result to be a substantial improvement over previous estimates, where isothermal instead of multithermal temperature distributions were used and no measurements of magnetically dissipated energies were available, resulting into a much lower estimate of the thermal energy content in the order of $E_{\rm th}/E_{\rm diss} \approx 0.2 - 1\%$ (Emslie et al. 2012). The thermal energy is smaller than the magnetically dissipated energy for essentially all events (Figure 8(a)), while the few mavericks can be explained by inaccurate energy measurements, either on the thermal or magnetic part. This result is certainly consistent with most magnetic reconnection models (where magnetic energy is converted into acceleration of particles) and the thick-target model (where the accelerated particles lose their energy by precipitation down to the chromosphere and heat up the chromospheric plasma). The amount of energy that goes into chromospheric and coronal plasma heating may well be larger than the thermal energy measured here, because we measured only the thermal energy content at the peak time of the flare, while multiple heating phases may occur before and after the flare peak. Even if we would add up all thermal energies from every flare episode that shows a subpeak in the soft or hard X-ray time profile, we would still underestimate the thermal energy because (radiative and conductive) cooling processes are not considered in the calculation of the thermal energy content here. Thus, the multithermal energy content calculated here represents only a lower limit of the heating energy that goes into flare plasma heating during a flare. A complete calculation of the multithermal flare energy would require a forward-fitting method of the evolution of the heating rate dE_h/dt that fits the observed conductive $dE_{\rm cond}/dt$ and radiative energy loss rate $dE_{\rm rad}/dt$, which is beyond the scope of this study, since this would require realistic geometric 3D models of flare loop arcades also.

5. CONCLUSIONS

As part of a global flare energetics study that encompasses all forms of energies that are converted during solar flares (with or without coronal mass ejections (CMEs)) we calculated the dissipated magnetic energy of 172 *GOES* M- and X-class events (in Paper I), and the multithermal energy at the peak time of 391 flare events (in this Paper II). The catalog of these flare events is available online, see http://www.lmsal.com/~aschwand/RHESSI/ flare_energetics.html. The major results of this study are:

1. We computed the DEM distribution function of all 391 flares in time steps of $\Delta t = 0.1$ hr using the spatially-synthesized Gaussian DEM forward-fitting method, which yields a detailed shape of the multithermal DEM distribution. This method is found to be robust and converges as a function of the macro-pixel size to a unique DEM solution, subject to uncertainties in terms of the instrumental response function and subtracted background fluxes in the order of ≈10%. The multithermal DEM function yields a significantly higher (typically by a factor of ≈14, but comprehensive, (multi-)thermal energy than the isothermal energy estimated from the same data.
2. For the overlapping dataset of 171 flare events for which we could calculate both the magnetically dissipated energies $E_{\rm diss}$ and the multithermal energies $E_{\rm th}$, we find a ratio of $E_{\rm th}/E_{\rm diss} \approx 2$–40%. This value is about an order of magnitude higher than previous estimates, i.e., $E_{\rm th}/E_{\rm diss} \approx 0.2$–1.0%, where isothermal energies from *GOES* X-ray data rather than multithermal energies from EUV AIA data were calculated, and a ratio of $E_{\rm diss}/E_p = 30\%$ was assumed ad hoc (Emslie et al. 2012).
3. The computed thermal energies are consistent with the RTV scaling law $E_{\rm th,RTV} = 7.3 \times 10^{-10}\, T_p^3 L_p^2$, which applies to the energy balance between the heating and (conductive and radiative) cooling rate at the turning point of the flare peak time. In our analyzed dataset of M- and X-class flares we find thermal energies in the range of $E_{\rm th} = 10^{28.3}$–$10^{32.0}$ erg. In comparison, the largest historical flare event has been reported to have an energy of $E_{\rm th} \approx 10^{33}$ erg, while the smallest coronal nanoflares with a length scale of $L_{\rm min} \gtrsim 1$ Mm and coronal temperature of $T_e \gtrsim 1$ MK are predicted to have values of $E_{\rm th} \gtrsim 10^{24}$ erg according to the RTV scaling law.
4. The size distributions of the spatial parameters display a powerlaw tail with powerlaw slopes of $\alpha_L^{\rm obs} = 3.3 \pm 0.3$ for the length scales, $\alpha_V^{\rm obs} = 1.7 \pm 0.2$ for flare volumes, $\alpha_E^{\rm obs} = 1.8 \pm 0.2$ for flare volumes, and are consistent with the predictions of the FD-SOC model combined with the RTV scaling law ($\alpha_L = 3.0$; $\alpha_V = 1.67$; $\alpha_E = 1.88$).

After we have established the measurements of magnetically dissipated flare energies (Paper I) and the multithermal energies (this paper), we plan to measure the non-thermal energies (using *RHESSI*), the kinetic energies of CMEs (using AIA/*SDO* and *STEREO*), and the various radiative energies in gamma-rays, hard X-rays, soft X-rays, EUV, and bolometric luminosity in future studies. The ultimate goal is to quantify and understand the energy partition in a comprehensive set of large flare/CME events, and to identify the physical processes that are consistent with the various flare energy measurements.

We appreciate helpful and constructive comments from an anonymous referee and from a number of participants of the RHESSI-13 workshop. Part of the work was supported by NASA contract NNG 04EA00C of the SDO/AIA instrument and the NASA STEREO mission under NRL contract N00173-02-C-2035.

APPENDIX
THERMAL ENERGY OF A MULTITHERMAL DEM

Thermal energies of solar flares are generally estimated by the expression for a homogeneous and isothermal plasma

(Equation (11)),

$$E_{\rm th} = 3 n_p k_B T_p V = 3 k_B T_p \sqrt{{\rm EM}_p\ V}, \quad \text{(A1)}$$

where $n_p = {\rm EM}_p/V$ is the electron density, T_p the electron temperature, and V the volume, measured at the peak time t_p of a flare. The values ${\rm EM}_p$ and T_p are generally determined from the peak in a DEM distribution function.

However, since the solar flare plasma is inhomogeneous and multithermal, we can calculate a more accurate expression for the total thermal energy when imaging observations are available. Ideally, such as in the case of an MHD simulation, the full 3D distributions of temperatures $T_e(x, y, z)$ and electron densities $n_e(x, y, z)$ are known, so that the most accurate expression for thermal energies can be computed by volume integration (e.g., Testa et al. 2012),

$$E_{\rm th} = \int\int\int 3 n_e(x, y, z) k_B T_e(x, y, z)\ dx\ dy\ dz. \quad \text{(A2)}$$

For numerical computations, we use a discretized 3D volume (x_i, y_j, z_k) that is aligned in the z-direction with the line-of-sight, while images in different wavelengths have the 2D coordinate system (x_i, y_i) with pixel size $\Delta x = \Delta y$. A DEM analysis yields an inversion of a DEM distribution ${\rm DEM}_{ij}(T) = {\rm DEM}(T; x_i, y_j)$ in every pixel at location (x_i, y_j). The column depth emission measure is defined by

$${\rm EM}_{ij} = \int {\rm DEM}_{ij}(T)\ dT = \int n_{ij}^2\ dz = n_{ij}^2\ L \quad \text{(A3)}$$

which yields an average density n_{ij} along the line-of-sight column depth with length L at each pixel position (x_i, y_j). We can then define a thermal energy $E_{{\rm th},ij}$ for each column depth $L = V^{1/3}$ by summing all contributions ${\rm EM}_k$ from each temperature interval ΔT_k (Equation (11)),

$$\begin{aligned} E_{th,ij} &= \sum_k 3 k_B V^{1/2} T_{ijk}\ {\rm EM}_{ij}^{1/2} \\ &= 3 k_B V^{1/2} \sum_k T_k \left[{\rm DEM}_{ij}(T_k)\ \Delta T_k\right]^{1/2}. \end{aligned} \quad \text{(A4)}$$

The total thermal energy in the computation box can then be obtained by summing up the partial thermal energies ${\rm EM}_{ij}$ from all pixels,

$$\begin{aligned} E_{\rm th} &= \sum_i \sum_j E_{th,ij} \Delta x^2 \\ &= 3 k_B V^{1/2} \sum_i \sum_j \sum_k T_k \left[{\rm DEM}_{ij}(T_k)\ \Delta T_k\right]^{1/2} \Delta x^2 \\ &= 3 k_B V^{1/2} \sum_k T_k \left[\sum_i \sum_j {\rm DEM}_{ij}(T_k)\ \Delta T_k\right]^{1/2} \Delta x^2 \\ &= 3 k_B V^{1/2} \sum_k T_k \left[{\rm DEM}(T_k)\ \Delta T_k\right]^{1/2}, \end{aligned} \quad \text{(A5)}$$

where we replaced the partial DEM functions ${\rm DEM}_{ij}(T_k)$ per column depths by the total DEM function ${\rm DEM}(T_k)$,

$${\rm DEM}(T_k) = \sum_i \sum_j {\rm DEM}_{ij}(T_k) \Delta x^2, \quad \text{(A6)}$$

which leads to the expression given in Equation (12).

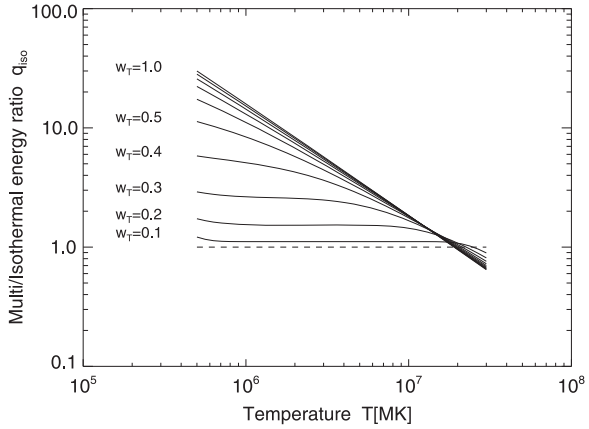

Figure A1. The thermal energy ratio $q_{\rm iso} = E_{\rm th,multi}/E_{\rm th,iso}$ is computed for narrow and broad single-Gaussian DEM distributions, with logarithmic temperature half widths (Equation (1)) in the range of $w_T \approx 0.1$–1.0.

We compare now the thermal energy $E_{\rm th}$ (Equation (A5)) computed in this way for a multithermal DEM distribution with the isothermal approximation (Equation (A1)) by their ratio in Figure A1 , given for a set of thermal widths $w_T = 0.1, 0.2, \ldots, 1.0$ in the single-Gaussian DEM function (Equation (1)) that is used for DEM modeling in each pixel. For small values, say $w_T = 0.1$, the DEM distributions are almost isothermal, and thus the approximation (Equation (A1)) is appropriate and we obtain a ratio near unity $q_{\rm iso} = (E_{\rm iso}/E_{\rm multi}) \gtrsim 1$). For broader multithermal DEM functions, the ratio increases systematically, up to a factor of $q_{\rm iso} \lesssim 30$. At higher temperatures, the ratio decreases because the temperature range between the peak of the DEM and the upper limit (here at $T = 30$ MK) becomes increasingly smaller and thus has less weight in the asymmetric T-weighting of the thermal energy contributions. Observed DEM peaks have typically a logarithmic temperature half width of $w_T \approx 0.5$ (see Figure 4 for examples), and thus the multithermal energy ratios vary by a factor of $q_{\rm iso} \approx 2 - 8$ for flare peak temperatures in the range of $T_p \approx 1 - 10$ MK (Figure A1). Since the observed DEM distributions are generally multi-peaked, the ratios tend to be higher than estimated from single-Gaussian DEMs as shown in Figure (A1).

REFERENCES

Aschwanden, M. J., & Benz 1997, ApJ, 480, 839
Aschwanden, M. J., Tarbell, T., Nightingale, R., et al. 2000, ApJ, 535, 1047
Aschwanden, M. J., & Parnell, C. E. 2002, ApJ, 572, 1048
Aschwanden, M. J., & Aschwanden, P. D. 2008, ApJ, 674, 530
Aschwanden, M. J., & Aschwanden, P. D. 2008, ApJ, 674, 544
Aschwanden, M. J., & Tsiklauri, D. 2009, ApJS, 185, 171
Aschwanden, M. J., & Boerner, P. 2011, ApJ, 732, 81
Aschwanden, M. J. 2012, A&A, 539, A2
Aschwanden, M. J., & Shimizu, T. 2013, ApJ, 776, 132
Aschwanden, M. J., Boerner, P., Schrijver, C. J., & Malanushenko, A. 2013, SoPh, 283, 5
Aschwanden, M. J., Xu, Y., & Jing, J. 2014a, ApJ, 797, 50
Aschwanden, M. J., Crosby, N., Dimitropoulou, M., et al. 2014b, SSRv, in press,
Bak, P., Tang, C., & Wiesenfeld, K. 1987, PhRvL, 59/4, 381
Bevington, P. R., & Robinson, D. K. 1992, Data Reduction and Error Analysis for the Physical Sciences (Boston, MA: McGraw Hill)
Boerner, P., Edwards, C., Lemen, J., et al. 2012, SoPh, 275, 41
Boerner, P. F., Testa, P., Warren, H., Weber, M. A., & Schrijver, C. J. 2014, SoPh, 289, 2377

Carmichael, H. 1964, in The Physics of Solar Flares, Proc. AAS-NASA Symp, NASA Special Publ. 50 ed. W. N. Hess (Washington, DC: NASA Science and Technical Information Division)
Caspi, A., Krucker, S., & Lin, R. P. 2014, ApJ, 781, 43
Craig, I. J. D., & Brown, J. C. 1976, A&A, 49, 239
Crosby, N. B., Aschwanden, M. J., & Dennis, B. R. 1993, SoPh, 143, 275
DeRosa, M. L., Schrijver, C. J., Barnes, G., et al. 2009, ApJ, 696, 1780
Emslie, A. G., Kucharek, H., Dennis, B. R., et al. 2004, JGRA, 109, A10 A10104
Emslie, A. G., Dennis, B. R., Holman, G. D., & Hudson, H. S. 2005, JGRA, 110, 11103
Emslie, A. G., Dennis, B. R., Shih, A. Y., et al. 2012, ApJ, 759, 71
Judge, P. G., Hubeny, V., & Brown, J. C. 1997, ApJ, 475, 275
Hirayama, T. 1974, SoPh, 34, 323
Kopp, R. A., & Pneuman, G. W. 1976, SoPh, 50, 85
Krucker, S., & Benz, A. O. 2000, SoPh, 191, 341
Lemen, J. R., Title, A. M., Akin, D. J., et al. 2012, SoPh, 275, 17
O'Dwyer, B., DelZanna, G., Mason, H. E., Weber, M. A., & Tripathi, D. 2010, A&A, 521, A21
Pallavicini, R., Serio, S., & Vaiana, G. S. 1977, ApJ, 216, 108
Parnell, C. E., & Jupp, P. E. 2000, ApJ, 529, 554
Pesnell, W. D., Thompson, B. J., & Chamberlin, P. C. 2011, SoPh, 275, 3
Rosner, R., Tucker, W. H., & Vaiana, G. S. 1978, ApJ, 220, 643
Ryan, D. F., O'Flannagain, A. M., Aschwanden, M. J., & Gallagher, P. T. 2014, SoPh, 289, 2547
Schrijver, C. J., Beer, J., Baltensperger, U., et al. 2012, JGRA, 117, 8103
Shimizu, T. 1997, PhD thesis, Univ. Tokyo
Shimojo, M., & Shibata, K. 2000, ApJ, 542, 1100
Sturrock, P. A. 1966, Natur, 5050, 695
Testa, P., de Pontieu, B., Martinez-Syjkora, J., Hansteen, V., & Carlsson, M. 2012, ApJ, 758, 54